

# Physical limits of cell migration: Control by ECM space and nuclear deformation and tuning by proteolysis and traction force

Katarina Wolf,<sup>1</sup> Mariska te Lindert,<sup>1</sup> Marina Krause,<sup>1</sup> Stephanie Alexander,<sup>3</sup> Joost te Riet,<sup>2</sup> Amanda L. Willis,<sup>4</sup> Robert M. Hoffman,<sup>5,6</sup> Carl G. Figdor,<sup>2</sup> Stephen J. Weiss,<sup>4</sup> and Peter Friedl<sup>1,3,7</sup>

<sup>1</sup>Department of Cell Biology and <sup>2</sup>Department of Tumor Immunology, Radboud University Nijmegen Medical Centre, 6500 HB Nijmegen, Netherlands

<sup>3</sup>David H. Koch Center for Applied Research of Genitourinary Cancers, Department of Genitourinary Medical Oncology, The University of Texas MD Anderson Cancer Center, Houston, TX 77030

<sup>4</sup>Division of Molecular Medicine & Genetics, Department of Internal Medicine, and the Life Sciences Institute, University of Michigan, Ann Arbor, MI 48109

<sup>5</sup>AntiCancer Inc., San Diego, CA 92111

<sup>6</sup>Department of Surgery, University of California, San Diego, La Jolla, CA 92103

<sup>7</sup>Cancer Genomics Center, 3584 CG Utrecht, Netherlands

Cell migration through 3D tissue depends on a physicochemical balance between cell deformability and physical tissue constraints. Migration rates are further governed by the capacity to degrade ECM by proteolytic enzymes, particularly matrix metalloproteinases (MMPs), and integrin- and actomyosin-mediated mechanocoupling. Yet, how these parameters cooperate when space is confined remains unclear. Using MMP-degradable collagen lattices or nondegradable substrates of varying porosity, we quantitatively identify the limits of cell migration by physical arrest. MMP-independent

migration declined as linear function of pore size and with deformation of the nucleus, with arrest reached at 10% of the nuclear cross section (tumor cells, 7  $\mu\text{m}^2$ ; T cells, 4  $\mu\text{m}^2$ ; neutrophils, 2  $\mu\text{m}^2$ ). Residual migration under space restriction strongly depended upon MMP-dependent ECM cleavage by enlarging matrix pore diameters, and integrin- and actomyosin-dependent force generation, which jointly propelled the nucleus. The limits of interstitial cell migration thus depend upon scaffold porosity and deformation of the nucleus, with pericellular collagenolysis and mechanocoupling as modulators.

## Introduction

Cell migration along and through 3D extracellular matrix (ECM) is fundamental to tissue formation and regeneration, immune cell trafficking, and disease, including cancer invasion and metastasis. Interstitial migration is a cyclic multi-step process consisting of (1) actin polymerization-dependent pseudopod protrusion at the leading edge; (2) integrin-mediated adhesion to ECM; (3) contact-dependent ECM cleavage by cell surface proteases; (4) actomyosin-mediated contraction of the cell body increasing longitudinal tension; and (5) rear retraction and translocation of the cell body (Ridley et al., 2003; Friedl and Wolf, 2009; Friedl and Alexander, 2011). This program is constitutively active in mesenchymal cells, including fibroblasts and solid tumor cells (Wolf et al., 2007; Sanz-Moreno et al., 2008; Sabeh et al., 2009;

Grinnell and Petroll, 2010), which display prominent protrusions and spindle-shaped morphology, strong adhesion to ECM, and proteolytic tissue remodeling. In contrast, interstitial leukocyte movement is characterized by an ellipsoid, rapidly deforming morphology with small protrusions, weak adhesion, and lack of proteolysis (Wolf et al., 2003b; Sabeh et al., 2009). Consequently, each step is considered adaptive in response to cell-intrinsic and extracellular chemical or mechanical signals, including regulators of adhesion, cytoskeletal dynamics, proteolysis, deformation of the cell body, and/or ECM geometry (Berton et al., 2009; Lautenschläger et al., 2009; Friedl and Wolf, 2010; Friedl et al., 2011; Tong et al., 2012).

Interstitial invasion of mesenchymal cells, including fibroblasts and tumor cells into collagen-rich ECM is controlled by

Correspondence to Katarina Wolf: [k.wolf@ncmls.ru.nl](mailto:k.wolf@ncmls.ru.nl); or Peter Friedl: [p.friedl@ncmls.ru.nl](mailto:p.friedl@ncmls.ru.nl)

Abbreviations used in this paper: AFM, atomic force microscopy; MLC, myosin light chain; MMP, matrix metalloproteinase; MT1-MMP, membrane-anchored 1-MMP; PMN, polymorphonuclear neutrophil.

© 2013 Wolf et al. This article is distributed under the terms of an Attribution–Noncommercial–Share Alike–No Mirror Sites license for the first six months after the publication date (see <http://www.rupress.org/terms>). After six months it is available under a Creative Commons license (Attribution–Noncommercial–Share Alike 3.0 Unported license, as described at <http://creativecommons.org/licenses/by-nc-sa/3.0/>).

Supplemental Material can be found at:  
[/content/suppl/2013/06/23/jcb.201210152.DC1.html](http://content.suppl/2013/06/23/jcb.201210152.DC1.html)  
 Original image data can be found at:  
<http://jcb-dataviewer.rupress.org/jcb/browse/6403>

MMPs (matrix metalloproteinases), particularly membrane-tethered (MT)1-MMP/MMP-14 as the key enzyme degrading intact fibrillar collagen (Sabeh et al., 2004; Wolf et al., 2007; Rowe and Weiss, 2009). Active MT1-MMP focalizes at contacts to collagen and cleaves fibrils that act as barriers to migration, particularly at pseudopod branches and along the cell body, and inhibition of MT1-MMP abrogates collagen cleavage and ECM remodeling (Sabeh et al., 2004; Wolf et al., 2007). As a consequence, nonproteolytic migration is either maintained by amoeboid cell deformation (Wolf et al., 2003a) or is abrogated (Sabeh et al., 2004), dependent on the type of collagen scaffold used as migration substrate (Packard et al., 2009; Sodek et al., 2008; Sabeh et al., 2009). Scaffolds reconstituted from different collagen sources vary in physicochemical properties, including porosity and stiffness (Zaman et al., 2006; Sabeh et al., 2009; Wolf et al., 2009; Yang and Kaufman, 2009; Miron-Mendoza et al., 2010; Yang et al., 2010). However, an integrative concept as to how ECM properties either allow or restrict migration as a function of MMP activity is lacking.

Here, we address the rate-limiting substrate conditions that enable or preclude the migration of different cell types in 3D extracellular matrices. Using live-cell microscopy, we first monitored migration rates and the associated deformation of both the cell body and nucleus in 3D matrices that range from low to high density. After mapping the subtotal and absolute migration limits, we then addressed important molecular modulators of migration efficacy in confined space. By multi-parameter analyses, we identify the ratio between ECM density and cell deformation as the key parameters controlling cell migration in dense tissue environments, with MMP activity, actomyosin-based contractility, and integrin-mediated mechanocoupling as modulators of invasion efficacy.

## Results

### **In vitro reconstitution of collagen matrices**

3D hydrogels were reconstituted from either telopeptide-intact covalently cross-linked collagen after acid extraction of rat tail tendon or telopeptide- and crosslink-reduced bovine dermal collagen after acid and pepsin treatment (Wolf et al., 2003a; Sabeh et al., 2004; Sodek et al., 2007; Packard et al., 2009). Equal collagen concentrations (1.7 mg/ml) were compared for assembly speed, fibril architecture, porosity, and matrix stiffness. For controlled culture and imaging conditions, the matrices were anchored using a custom glass chamber (Fig. S1 A). Time-to-polymerization monitored by confocal backscatter microscopy at 37°C yielded 16-fold faster assembly of rat tail (half-maximum polymerization after 30 s) relative to bovine dermal collagen (8 min; Fig. 1 A). The different assembly speeds are consistent with the divergent telopeptide contents of the collagen preparations (Helseth and Veis, 1981; Sabeh et al., 2009). The fibrillar matrix architecture, as detected by confocal reflection microscopy, was verified by collagen type-I immunofluorescence, hence confirming a negligible detection error from backscatter-negative fibrils in vertical orientation (below 3% of signal-containing pixels; Fig. S1, B–D; Jawerth et al., 2010). Whereas rat tendon-derived collagen formed thin fibrils

with a 20-nm diameter and a narrow pore size range of 2–5  $\mu\text{m}^2$  (1–2  $\mu\text{m}$  pore diameters), bovine dermis-derived collagen matrices were comprised of fibrils with a diameter of 60 nm and pore cross sections ranging from 6–30  $\mu\text{m}^2$  (2–6  $\mu\text{m}$  pore diameters; Fig. 1 B, D, E; Fig. S2 A, B, D, and E). The fractal box count, measured as fibril-containing fields of decreasing side length, was two- to threefold higher for rat tail collagen compared with concentration-matched bovine collagen (Fig. S2, C and F). To control for fibril density-dependent changes in collagen lattice stiffness, atomic force microscopy (AFM) was used with a 10- $\mu\text{m}$  bead as probe to approximate the size of a cell. The surface of the lattice was repeatedly probed by the cantilever (Fig. S1 A) and both bead penetration and force were co-registered (Fig. 1 C, left). Consistent with previous reports, AFM revealed a twofold lower elastic modulus for bovine dermal compared with rat tail collagen at 1.7 mg/ml (28 vs. 51 Pa; Fig. 1 C, right; Stein et al., 2008; Yang and Kaufman, 2009). Thus, although reconstituted at equivalent concentrations, the collagen preparations substantially diverge in terms of fibril diameter and interfibrillar space, and moderately in network stiffness.

### **Pore size dependence of proteolytic and nonproteolytic migration of HT1080 cells**

To recapitulate differences in MMP-independent cell migration rates between the collagen preparations, MT1-MMP-transduced HT1080 (HT/MT1) cells were used as model for efficient collagenolytic invasion converting to collagenolysis-independent migration after broad-spectrum MMP inhibition with GM6001 or MT1-MMP silencing (Wolf et al., 2007; Sabeh et al., 2009). Baseline migration of HT/MT1 cells reached 0.7  $\mu\text{m}/\text{min}$  in bovine dermal and 0.3  $\mu\text{m}/\text{min}$  in rat tail collagen lattices at 1.7 mg/ml collagen content (Fig. 2, A and C; Video 1 A), suggesting that MMPs enable migration in collagen scaffolds of diverging pore size. Conversely, broad-spectrum MMP inhibition by GM6001 prompted cell immobilization in rat tail but not bovine dermal collagen in three different migration models (Fig. S1 A), including individual cell migration quantified by cell tracking (Fig. 2, A and C; Video 1 B), cell emigration from multicellular spheroids (Fig. S3 A and B [top]; and C [top]; Video 3), and vertical invasion after cell seeding atop 3D collagen lattices (Fig. S3 D). Equivalent inhibition of migration was obtained by transient knockdown of MT1-MMP expression, confirming MT1-MMP as the invasion-promoting collagenase (Fig. S3 B, bottom; Sabeh et al., 2009).

To test whether divergence of MMP-independent migration arises as a function of fibril density, matrix porosity was normalized by varying the collagen content. Increasing the concentration of bovine dermal collagen from 1.7 to 15 mg/ml resulted in significantly smaller pore cross sections (median 5  $\mu\text{m}^2$ ; Fig. 1 D; Fig. S2, A–C), higher stiffness (shown for a bovine lattice of 6.6 mg/ml; Fig. 1 C), and a dose-dependent migration delay, ultimately resulting in the immobilization of HT/MT1 cells in the presence of GM6001 (Fig. 2 A). To categorize this graded response, we operationally defined subtotal and absolute migration limits as 90 and 99% speed delay, respectively. Impeded migration in bovine dermal collagen was a linear function of the

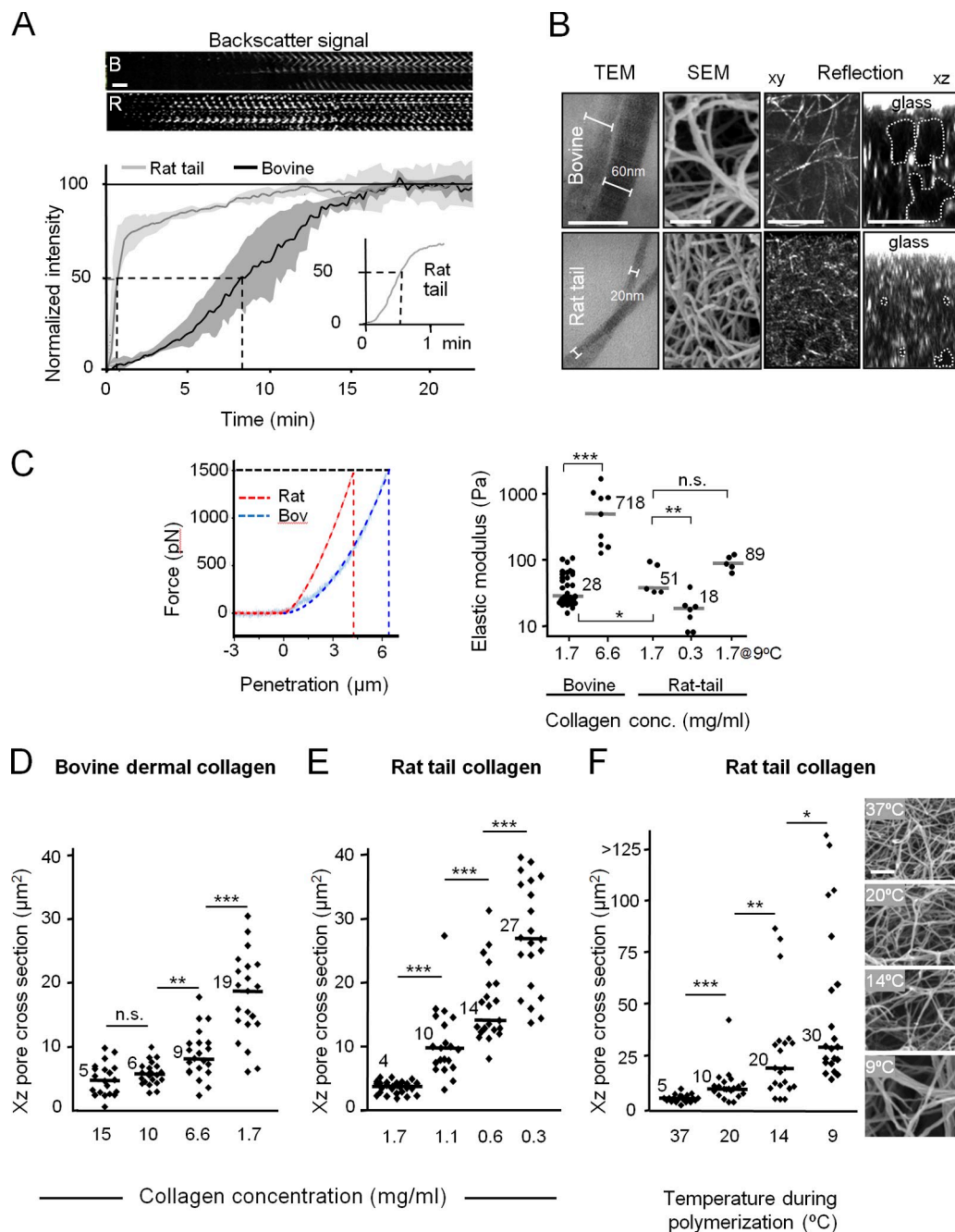


**Figure 1. 3D collagen lattices of varying origin and cross-link status: Assembly speed, stiffness, and pore sizes at different polymerization conditions.**

(A) Assembly speed and (B) organization of acid-extracted pepsinized bovine dermal compared with acid-extracted rat tail collagen matrices after *in vitro* reconstitution (1.7 mg/ml). (A) Real-time confocal reflection microscopy of fibril formation, represented as kymograph (top panel; B, bovine dermal collagen; R, rat tail collagen) and time-dependent signal intensity curves normalized to the end-point of complete polymerization (bottom panel, horizontal solid line;  $n = 3 \pm \text{SD}$ , shaded areas). Dashed lines, half-maximal polymerization after 8 min (bovine) and 30 s (rat tail, also see inset). (B) Collagen fibril diameter and network geometry, detected by transmission and scanning electron microscopy (TEM, SEM) of fixed dehydrated lattices and confocal reflection microscopy (horizontal, xy; vertical, xz) of native hydrated samples. Marked areas in xz represent signal-free regions referred to as pores. Brackets (TEM) indicate representative fibril calibers. (C) Determination of elastic modulus of bovine and rat tail collagen lattices by AFM. Left, force curves while probing bovine dermal or rat tail collagen lattices (1.7 mg/ml). Dotted curves, medians of all values fitted by the Hertz formula. Oscillatory example curves represent each one of 5–35 repeats. Vertical lines, deformation depth at 1,500 pN applied force. Right, stiffness for different collagen types and concentrations. Unless stated otherwise, polymerization temperature was 37°C. \*\*\*,  $P < 0.0001$ ; \*\*,  $P < 0.01$ ; \*,  $P < 0.05$ ; n.s., not significant; data points represent 5–35 measurements from different locations as average of 2–20 repetitive tappings/position. Gray horizontal lines, median. (D–F) Pore cross sections quantified by confocal reflection xz sections of bovine dermal or rat tail collagen lattices of different polymerization conditions. Horizontal lines, medians. Data show 1–2 representative experiments from  $n = 3$ –4; 21 data points each. \*\*\*,  $P < 0.001$ ; \*\*,  $P < 0.01$ ; \*,  $P < 0.05$ ; n.s., nonsignificant. (F) Right column, SEM from rat tail collagen lattices assembled at different temperatures. Bars: (A; B, confocal reflection) 10  $\mu\text{m}$ ; (B, F, SEM) 1  $\mu\text{m}$ ; (B, TEM) 0.1  $\mu\text{m}$ .

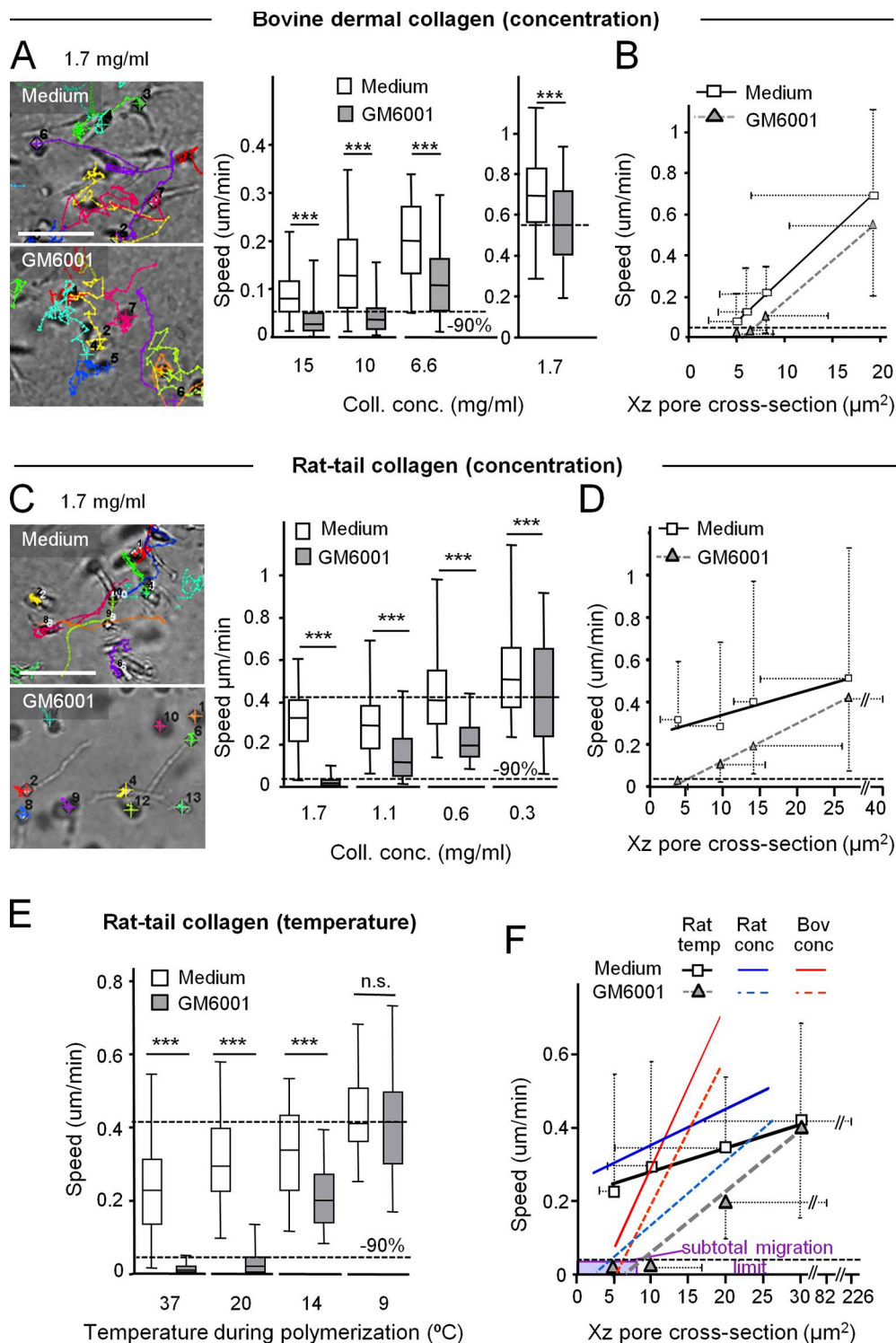


Figure 2. **Collagen pore size determines physical migration limits of HT/MT1 cells in 3D collagen lattices.** (A, C, and E) Single-cell migration rates in bovine dermal or rat tail collagen lattices of varying concentration or polymerization temperature (1.7 mg/ml) using anchored 3D matrices in migration chambers (shown in Fig. S1 A), monitored by time-lapse microscopy and analyzed by single-cell cell tracking. Migration paths (A and C, left) and averaged single-cell speeds (A and C, right; E) after 24 h of observation in the absence or presence of MMP inhibitor GM6001. Horizontal lines and boxes and whiskers show the medians, 25th/75th, and 5th/95th percentile (50–180 cells, 19–24 h of migration analyzed, 3–6 independent experiments). Dashed lines indicate references for 100% MMP-independent movement and 90% inhibition. \*\*\*,  $P < 0.0001$ ; n.s., not significant. (B, D, and F) Correlation between median pore cross section (from Fig. 1, D–F) and proteolytic and MMP-independent cell speed (A, C, and E) for each collagen condition. Symbols show medians, and whiskers the 5th/95th percentiles.  $R^2$  (describing how well the regression line approximates real data points), slopes, and significance between slopes from untreated and GM6001-treated populations were as follows: (B) bovine dermal collagen, untreated control 0.998/0.044; GM6001-treated population 0.991/0.040/n.s.; (D) rat tail collagen, untreated control 0.851/0.010, GM6001-treated cells 0.999/0.017/\*,  $P < 0.05$  ( $P = 0.045$ ); (F) rat tail collagen with varied polymerization temperature, untreated control 0.960/0.007, GM6001-treated cells 0.972/0.017/\*,  $P < 0.05$  ( $P = 0.01$ ). Dashed lines, 90% inhibition of migration. Bars: (A and C) 100  $\mu\text{m}$ .

pore size for both MMP-mediated and MMP-independent migration with similar slope, but higher offset with MMPs available (Fig. 2 B). Conversely, decreasing the concentration of rat tail collagen to a minimum of 0.3 mg/ml, which lowers scaffold stiffness (Fig. 1 C) but provides larger pore cross sections of 20–30  $\mu\text{m}^2$  (Fig. 1 E; Fig. S2, D–F), fully rescued MMP-independent migration, eventually reaching the speed distribution of control cells (Fig. 2 C). Again, migration was a linear function of pore size, with a significantly steeper slope when MMP activity was inhibited (Fig. 2 D).

To avoid varying collagen concentrations, and to minimize indirect effects unrelated to porosity (e.g., altered density of adhesive ligands [Zaman et al., 2006] or uncontrolled collagen cross-link density in bovine dermal collagen), the porosity of rat tail collagen lattices was altered by reducing the polymerization temperature (Raub et al., 2007) while keeping collagen concentration constant (1.7 mg/ml). At 9°C, fibrillogenesis was delayed (Fig. S2 H, top) and, consequently, pore diameters and related cross sections increased (median diameter 8  $\mu\text{m}$  and median cross section 30  $\mu\text{m}^2$ ) and fractal box count decreased, while fibril diameter (80 nm) and stiffness increased (Fig. 1, C and F; Fig. S2, H [bottom] and L). Again, as pore size increased, MMP-independent migration in rat tail collagen was rescued with single-cell movement reaching peak speeds equal to proteolytic migration rates (Fig. 2 E; Video 4). This rescue was achieved as well for cell emigration from multicellular spheroids (Fig. S3 C) or vertical invasion cultures (Fig. S3 D). As before, the speed of MMP-independent migration was a linear function of pore size with a significantly steeper slope observed relative to protease-dependent migration rates (Fig. 2 F). Hence, irrespective of collagen preparation, the strategy used to alter pore size, or migration assay used, cell speed was a linear function of pore size. Notably, the availability of MMP activity was sufficient to maintain migration even when cells were confronted with small pores that otherwise impeded or arrested migration (Fig. 2 F).

#### **MMP-independent migration in dense ECM depends upon deformation of the nucleus**

To identify the subcellular compartments that modulate migration in dense 3D environments, the morphokinetic changes of cell body, leading edge, and nucleus were assessed as a function of collagen density. HT/MT1 cells embedded in bovine dermal collagen in the presence of GM6001 moved both their leading edge and cell bodies at approximately equal velocities. In contrast, after migration arrest in rat tail collagen, cells displayed an immobile spherical central body with one or more dynamic, dendrite-like extension (Fig. 3 A; Video 1 B) with zones of collagen deformation at the front pole (Video 2). In addition, pseudopods occasionally broke away from cell bodies and moved with snake-like morphology (Video 3 B, right). The arrested portion of the cell body consisted of cytoplasm and nucleus forming occasional small protrusions (prolapse) pointing toward the leading cell extension (Fig. 3, B and C; Video 2, arrow; Video 5). In arrested cells, nuclear prolapses measured 1–3  $\mu\text{m}$  in diameter (1–7  $\mu\text{m}^2$  cross section), whereas nuclei of cells during MMP-independent migration adopted hourglass deformations that were 3–7  $\mu\text{m}$  in diameter (7–40  $\mu\text{m}^2$  cross section;

Fig. 3, B–D). These morphological signatures were distinct from the ellipsoid nuclear shapes (8–11  $\mu\text{m}$  in diameter; 50–100  $\mu\text{m}^2$  in cross section) observed in MMP-competent HT1080 cells that generated proteolytic tracks whose widths match those of the cell diameter (Fig. 3, C and D). Accordingly, irrespective of the collagen preparation or scaffold porosity, the nuclear diameters of MT1-MMP-expressing control cells retained average cross sections of 40–90  $\mu\text{m}^2$  (Fig. 3 E). Conversely, GM6001 caused a gradual decrease of nuclear diameters until conditions of arrest were reached (Fig. 3 E), with either a singular small nuclear prolapse (Fig. 3 D; Fig. 3 E, pink dotted circles) or a nondeformed spherical shape (Fig. 3 D; Fig. 3 E, black dotted circles). These population data confirm time-lapse imaging data that show immobilized nuclei cycling between prolapse and rounding (Video 2). In summary, hourglass-shaped deformations of the nucleus are sufficient to maintain MMP-independent migration of HT/MT1 cells through 3D collagen lattices with pore diameters above 7  $\mu\text{m}^2$ , whereas smaller pore sizes defeat nuclear deformability and prompt physical arrest despite persistent leading edge kinetics and frustraneous force generation. Hence, MMP-independent migration in dense ECM depends upon deformation of the nucleus.

#### **Modulation of migration in confined space by cell actomyosin contractility and integrin-mediated mechanocoupling**

The combination of ongoing cytoskeletal activity and impaired migration suggests an active role for mechanocoupling in confined space. We therefore tested both integrin-mediated leading edge traction on substrate using  $\beta 1$  integrin-perturbing mAb 4B4 (Wolf et al., 2003a) and actomyosin-dependent contractility using ROCK inhibitor Y-27632 that inhibits myosin light chain (MLC) phosphorylation and contraction of the cell rear (Fig. 4 A; Ren et al., 2004; Lämmermann et al., 2008). Both approaches gradually impaired HT/MT1 cell-mediated contraction of collagen lattices (Fig. 4 B). Using collagen matrices with 20  $\mu\text{m}^2$  pore area, representing a moderate physical challenge to nuclear deformability (compare Fig. 1 D with Fig. 3 D), both mAb 4B4 and Y-27632 significantly delayed migration rates in a dose-dependent manner, with greater negative impact by GM6001 relative to control cells (Fig. 4 C). Mechanically perturbed force generation by mAb 4B4 was apparent from compromised cell elongation (Fig. 4 D). When mAb 4B4 was used at a concentration that inhibited collagen contraction by ~50% (1  $\mu\text{g}/\text{ml}$ ; see Fig. 4 B, left), MMP-independent migration was almost completely blocked, consistent with an impaired ability to generate sufficient adhesion and traction force to translocate the nucleus (Fig. 4 C and F; Video 6 A, left). Consequently, reducing space constraints by enlarging pore diameters to ~55  $\mu\text{m}^2$  (Fig. 4 E) led to a near-complete rescue of migration (Fig. 4 F; Video 6 A, middle and right). Consistent with the speed delay in constraining matrix (1.7 mg/ml bovine collagen in the presence of GM6001), increased nuclear deformation was observed that, again, could be reversed when matrix porosity was increased or MMPs were engaged (Fig. 4 G). With the integrin system intact, the importance of actomyosin-mediated cell contraction in propelling the nucleus through 3D matrix was underlined by

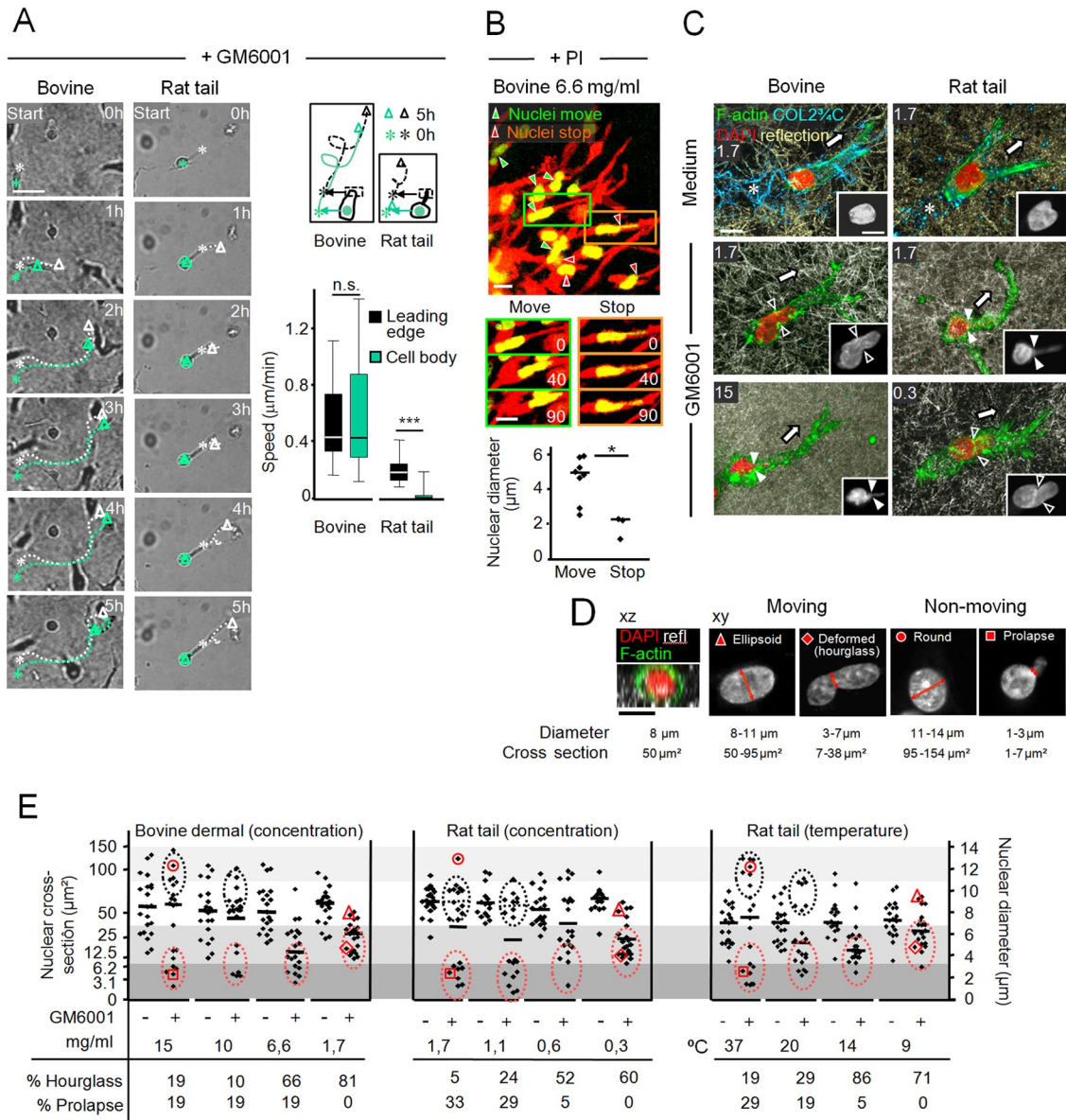


**Figure 3. Requirement for deformation of the nucleus during MMP-independent migration at rate-limiting pore conditions.** (A) Time-lapse sequence (left) and population speed (right) of leading edge and main cell body in bovine dermal and rat tail collagen (1.7 mg/ml) in the presence of GM6001. Tracking of the leading extension (white dotted lines) and body (green dotted lines) from starting (\*) to end (triangle) position after 5 h. Speed is depicted as median with box blot and whiskers (5th/95th percentile; 45 cells, 3 independent experiments). \*\*\*,  $P < 0.0001$ ; n.s., nonsignificant. (B) Nuclear deformation in moving or migration-arrested nuclei in HT1080 cells expressing H2B/EGFP and cytoplasmic DsRed2 in 6.6 mg/ml bovine dermal collagen in the presence of protease inhibitor cocktail (PI). Overview image from movie sequence (top; Video 5) highlighting moving (green arrowheads) and immobilized nuclei (red arrowheads). Middle: time-lapse example sequences of moving and immobilized nuclei from cells marked in the top image (numbers, time in min). Bottom: diameters of deformed nuclei from independent cells during migration or immobilization. 10 cells from one representative experiment out of  $n = 2$ ; \*,  $P < 0.05$ . (C) Morphology of cell body and nucleus during migration in 3D bovine dermal or rat tail collagen matrix (numbers, collagen concentration in mg/ml) in the absence or presence of GM6001. Cultures were fixed 10–16 h after polymerization and stained as indicated, including collagen cleavage neoepitope detection (cyan signal). Nuclear deformation imposed by collagen structures in moving cells in the presence of GM6001 (diameters 4–5  $\mu\text{m}$ ; empty arrowheads); conditions of immobilization induce nuclear rounding with occasional thin prolapse (white arrowheads). Arrows, direction of migration and protrusion, respectively. (D) Classification of nuclear morphologies under conditions of cell migration (middle) and immobilization (right). Left: representative xz cross section of a nondeformed HT/MT1 cell (50  $\mu\text{m}^2$ ). Arrows, nuclear diameters used for quantification in B and E. Numbers show arbitrary ranges for diameters and corresponding cross sections for each phenotype. Red symbols (top-left corner) represent population phenotypes marked in E. (E) Nuclear diameters from cells cultured in collagen matrices of varying pore sizes in the absence or presence of GM6001. After 16 h, samples were fixed, stained with DAPI and phalloidin, and cells with polarized morphologies were analyzed by confocal microscopy for nuclear diameters (compare C). Red dashed ovals, subset of deformed nuclei with hourglass shape associated with movement (middle gray zone) or local prolapse in largely arrested cells (dark gray zone). Black dashed ovals highlight round nuclei of arrested phenotypes (light gray zone). Horizontal lines represent the medians (of each 21 nuclei per group; 2–3 independent experiments). Tables indicate the frequency of hourglass and prolapse phenotypes for each condition. Bars: (A) 50  $\mu\text{m}$ ; (B–D) 10  $\mu\text{m}$ .

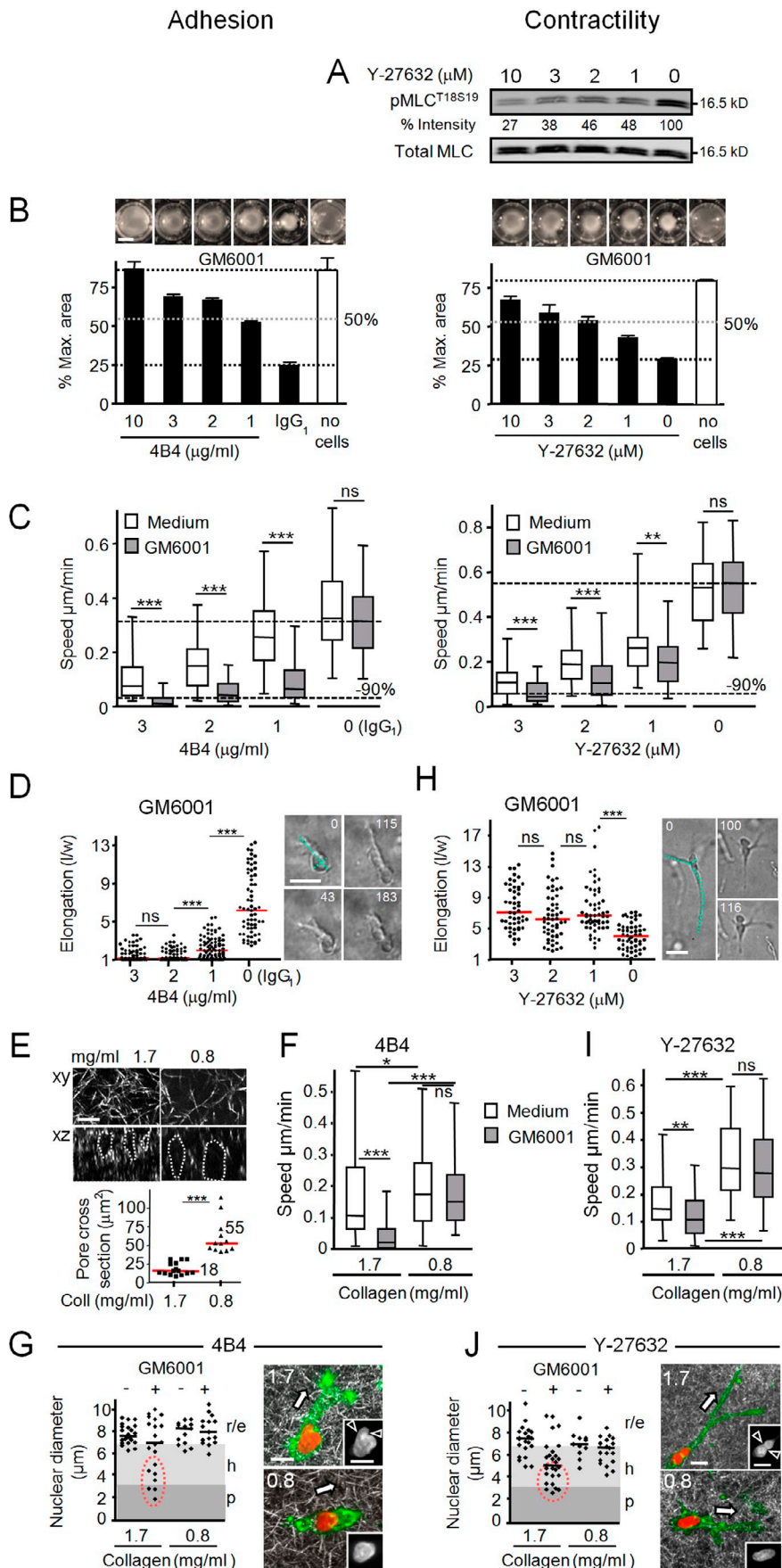


**Figure 4. Modulation of migration efficiency and nuclear deformation in dense collagen lattices by integrin- and actomyosin-mediated force generation.** (A) Dose-dependent reduction of pMLC<sup>T18S19</sup> content in the presence of ROCK inhibitor Y-27632 in HT/MT1 cells. Signal intensity was calculated by densitometry and normalized to the total MLC signal. (B) Dose-dependent inhibition of collagen contraction by anti- $\beta 1$  integrin mAb 4B4 (left) or Y-27632 (right). Cell-free and cell-containing collagen lattices treated with GM6001 (20  $\mu\text{M}$ ), and mAb 4B4, control IgG<sub>1</sub> (3  $\mu\text{g/ml}$ ), or Y-27632 at indicated concentration. Matrix contraction was measured from gel areas (top images) after 48 h (left) or 24 h (right) as triplicates (means and SD from one representative experiment). Dashed horizontal lines mark 0, 50, and 100% gel contraction. (C) Mean population speed from single-cell analysis after 19–24 h of cell tracking in bovine collagen (1.7 mg/ml) in the absence or presence of MMP inhibitor GM6001 (20  $\mu\text{M}$ ) and mAb 4B4 or Y-27632. Medians and boxes and whiskers from 60–150 cells ( $n=2-3$  for Y-27632;  $n=3-5$  for 4B4). Dashed lines indicate 100% reference for MMP-independent movement and 90% inhibition. \*\*\*,  $P < 0.0001$ ; \*\*,  $P < 0.01$ ; n.s., not significant. (D and H) Median elongation (cell body length divided by width) after 10 h of MMP-independent migration (50–90 cells from  $n=2$ ; \*\*\*,  $P < 0.0001$ ; n.s., not significant). Horizontal line, median. (E) xy and xz image cross sections of confocal reflectance from bovine collagen fibrils (top) and quantification of pore cross sections (1.7 vs. 0.8 mg/ml concentration). (F and I) Population speed from single-cell analysis in bovine dermal collagen in the presence of 1  $\mu\text{g/ml}$  mAb 4B4 (F) or 2  $\mu\text{M}$  Y-27632 (I) and, where indicated, 20  $\mu\text{M}$  GM6001. 60–108 cells from 2–3 independent experiments; \*\*\*,  $P < 0.0001$ ; \*\*,  $P < 0.01$ ; \*,  $P < 0.05$ ; n.s., non-significant. (G and J) Nuclear diameter analysis as described in the legend of Fig. 3 E. Red dashed ovals, subset of deformed nuclei with hourglass (“h”) shape associated with movement (middle gray zone) or local prolapse (“p”) in largely arrested cells (dark gray zone). r/e, round or ellipsoid nuclei. Arrowheads, deformation of nuclei; arrows, migration direction. Cells migrated in bovine collagen in the presence of either 1  $\mu\text{g/ml}$  4B4 antibody or 2  $\mu\text{M}$  Y-27632 and, when indicated, 20  $\mu\text{M}$  GM6001. 11–27 cells each;  $n=2$ . Bars: (B) 5 mm; (D) 25  $\mu\text{m}$ ; (E, G, and J) 10  $\mu\text{m}$ .

delayed rear retraction and increased cell length in the presence of Y27632 (Fig. 4 H; Video 6 B, left). A concentration causing half-maximum collagen contraction (Fig. 4 B, right), Y27632 (2  $\mu\text{M}$ ) effected a partial migration arrest and, concomitantly, strong nucleus deformation in the presence of GM6001 (Fig. 4, C, I, and J). Both of these inhibitors' effects were effectively reversed by increasing pore size cross sections (Fig. 4, I and J; Video 6 B, middle and right). Thus, both integrin-mediated traction force and actomyosin contractility are required to propel the nucleus forward when dense ECM is transmigrated in cooperation with MMP-mediated pore generation.

#### Divergent kinetics and rate-limits in mononuclear and polymorphonuclear cells

To obtain insight into how different nuclear shape types enable or limit migration in restricted space, we examined the nuclear mechanics of additional cell types with mononuclear or polymorphonuclear organization. Lamin A/C, a central nuclear protein required for nuclear membrane organization and stability (Goldberg et al., 2008), is expressed in tumor cells, including HT/MT1, HT/wt, and MDA-MB-231/MT1 (MDA/MT1) breast cancer cells, but not in human CD4+ T-blasts or polymorphonuclear neutrophils (PMNs; Fig. 5 A). Irrespective of cell type, migration of mononuclear cells through low- to intermediate-density collagen lattices remained unperturbed by GM6001 (Fig. 5, B and D; Fig. S4 A). Ongoing migration was accompanied by deformation of the nucleus with cross section distributions matching the available pore size range of the matrix (Fig. 5, C and E; Fig. S4 B). In HT/wt cells and T-blasts moving through dense matrices, hourglass nuclear shapes predominated, whereas MDA/MT1 cells displayed a spectrum from hourglass to cigar-like shapes. For pore dimensions ranging from 2 to 5  $\mu\text{m}^2$ , GM6001 caused migration arrest and nuclear prolapse formation in tumor cells, whereas T-blast migration persisted, albeit at slower speeds (Fig. 5, B–D; Fig. S4, A–C; Video 7). Compared with tumor cells, T-blasts are distinguished by a two- to fourfold smaller nucleus (Fig. 3 C; Fig. 5 E) and the inability to proteolytically degrade fibrillar collagen, thus constitutively depending upon shape changes alone to bypass matrix barriers (Wolf et al., 2003b). Ultimately, however, all T-blasts were immobilized at pore cross sections of 1–2  $\mu\text{m}^2$  (Fig. S2 G; Fig. 5 F) that no longer accommodated nuclear deformations (Fig. 5 E; Fig. S4 D). Thus, MMP-independent mononuclear cell migration uniformly depends upon nuclear deformation in response to lateral compression by tissue structures.

Similarly, PMN migration remained unaffected by the absence or presence of GM6001 in low- to intermediate-density collagen matrices (Fig. 5 F). In contrast to “in-whole” deformation of mononuclear nuclei, the segmented nucleus of PMNs displayed interconvertible folding states, including compact configuration or pearl chain-like complete or partial unfolding (Fig. 5 G). These folding states reflected speed changes, alternating between compaction during phases of immobility and unfolding during migration (Fig. 5 H; Fig. S4 E, example 1; Video 8). In high-density rat-tail collagen (3.3 mg/ml, pore cross section 2–3  $\mu\text{m}^2$ ), PMN migration remained intact irrespective of MMP activity, albeit at reduced speed, and was arrested at higher collagen density

(6.6 mg/ml) when pore cross sections decreased to 0.5–1.5  $\mu\text{m}^2$  (Fig. 5 F; Fig. S2 G; Video 7). Not unlike tumor cells, immobilized PMNs exhibited collapsed, spherical nuclei with occasional single-segment prolapse toward the leading oscillating pseudopod (Fig. 5, G and I; Fig. S4, F and G). In summary, stereotypic shape change patterns, as exemplified by hourglass-like compression of mononuclear nuclei or unfolding of polymorphonuclear nuclei, are sufficient to maintain cell navigation through interstitial matrices. In high-density fibrillar collagen matrix with collagenolysis absent, nuclear deformability alone determines migration rates as a function of pore size, reaching near absolute limits at 7  $\mu\text{m}^2$  in tumor cells and 2–3  $\mu\text{m}^2$  in PMNs and T-blasts (Fig. 6 A). Thus, impaired migration is a linear function of pore size and independent of scaffold stiffness (Fig. 6 B).

#### Physical limits of cell migration through nondegradable substrate

Migration rates through dense 3D collagen gels and broad-spectrum MMP inhibitor treatment might be affected by additional parameters not yet addressed, including residual low-level MMP-independent collagenolysis executed by other classes of proteases; guidance by occasional gaps and fissures present in randomly assembled bio-scaffolds; and/or mechanical rupture of very small or incompletely polymerized collagen fibrils by migrating cells. To exclude such interfering parameters, we used a polycarbonate filter model for cell trafficking through nondegradable and nondeformable barriers. In this system, sub-total inhibition (90%) of migration was reached at pore cross sections of 7–10  $\mu\text{m}^2$  for all mononuclear cell types and 4  $\mu\text{m}^2$  for PMN with complete inhibition (>99%) obtained at pore dimensions below 5–6  $\mu\text{m}^2$  for mononuclear cells and 1  $\mu\text{m}^2$  for PMNs (Fig. 7 A). Similar to 3D collagen matrices, effective transmigration through polycarbonate filter pores resulted from cytoplasmic protrusion followed by nuclear deformation within a pore cross-sectional range of 7–50  $\mu\text{m}^2$  (Fig. 7, B and C). Likewise, the morphology of cells immobilized above small pores (0.8  $\mu\text{m}^2$  cross section) consisted of a long cytoplasmic protrusion extending into and the nucleus atop the pore (Fig. 7, B and C), thereby recapitulating the arrested phenotypes observed in high-density fibrillar collagen. Thus, cell migration through nondegradable pores exhibits physical thresholds that are dependent upon pore size and nuclear deformability, confirming the limiting thresholds obtained for 3D fibrillar collagen matrix.

## Discussion

By challenging MMP-dependent and -independent cell movement with decreasing scaffold porosity, and by quantitatively co-registering migration speed with the shapes of cell body and nucleus, we have identified the rate-limiting physicochemical determinants of cell migration. First-order determinants are (1) the available spaces between ECM fibrils or within the filter pore that can accommodate the moving cell body and (2) the deformability of the nucleus in response to space constraints.

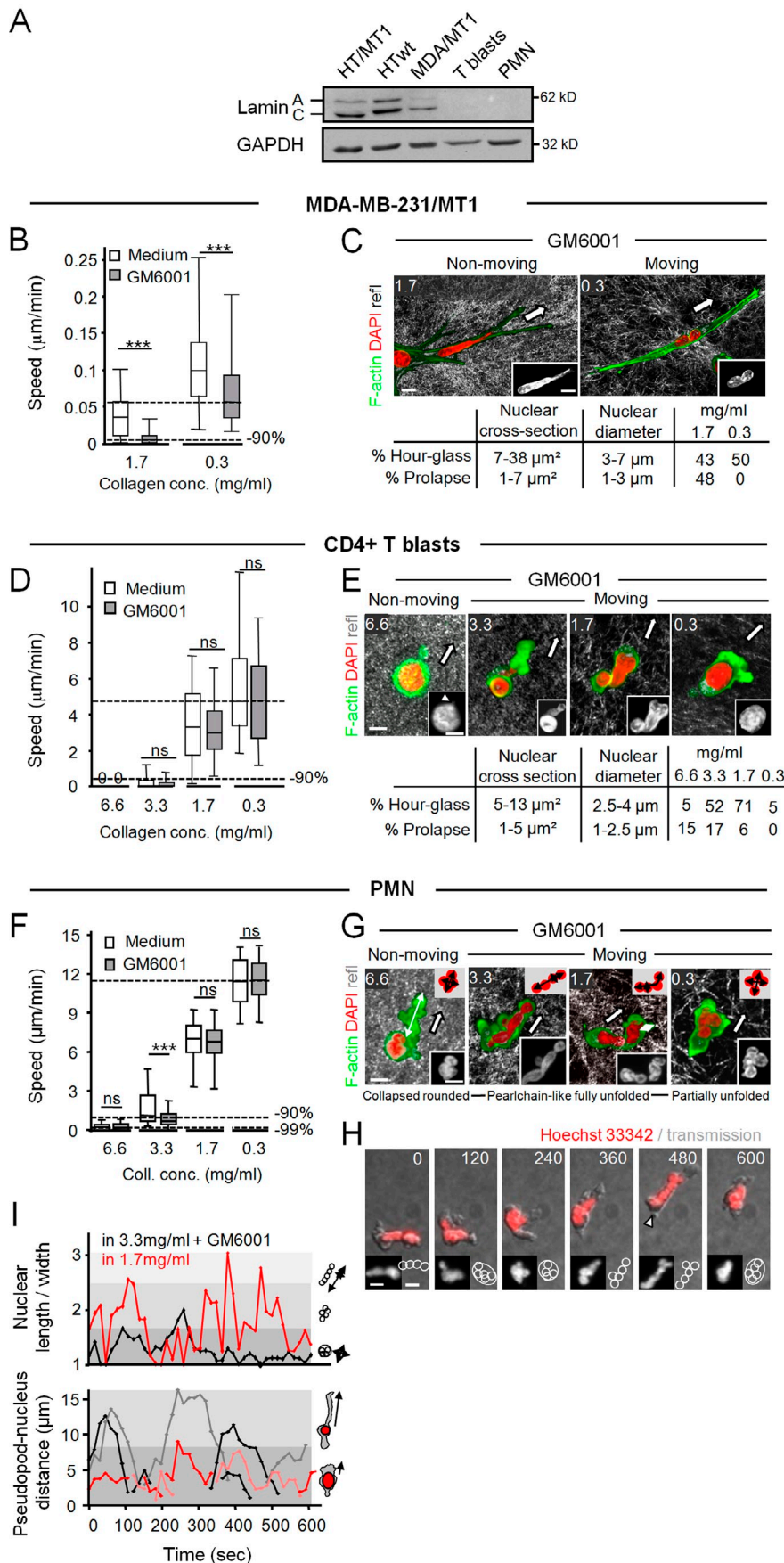


**Figure 5. Pore size-dependent migration and deformation of the nucleus in mononuclear breast cancer cells, T-blasts, and PMN.** (A) Lamin A/C content in distinct cell types. Lanes were loaded with whole-cell lysates normalized to GAPDH content and immunoblotted for lamin A/C. (B, D, and F) Migration efficiencies of the indicated cell types in rat tail collagen of different density in the absence or presence of GM6001. Steady-state speeds of single cells monitored over 24 h (MDA/MT1) or 2 h (T-blasts, PMNs). Dashed horizontal lines, subtotal (90% inhibition) and absolute (99% inhibition) migration limit (dashed top line indicating 100% of MMP-independent migration). Box and whiskers show the medians, 25th/75th and 5th/95th percentiles (50–200 cells, 2–6 independent experiments). \*\*\*,  $P < 0.0001$ ; n.s., not significant. (C, E, and G) Moving and immobilized phenotypes of MDA/MT1 cells, T-blasts, and PMN in the presence of GM6001 in rat tail collagen of different pore sizes (numbers, collagen concentration in mg/ml). Cultures were fixed at the end-point (16 h, MDA/MT1; 2 h, leukocytes) and stained as indicated. Insets, DAPI. Arrows, direction of migration and protrusion, respectively. Tables (C and E), ranges of nuclear cross sections and diameters and their frequencies at different collagen density (numbers in percent, full dataset shown in Fig. S4, C and D) associated with intact or abrogated migration (17–30 independent cells). Insets (G), schematics of different nuclear shapes, including rounded (immobilized), fully or partially unfolded. (H) Change of nuclear morphology in migrating PMN (rat tail collagen, 1.7 mg/ml) over 600-s time period (full sequence shown in Fig. S4 E, example 1; and Video 8). Insets, DAPI signal (left) and schematics of nuclear shape (right). Arrowhead, saltatory migration phase. (I) Nuclear elongation index (top graph) and distance between nucleus and leading extension (pseudopod–nucleus distance) plotted over time. Measurement as indicated by black arrows. Graphs show one representative example of a moving cell (red lines; compare to Fig. S4 E, example 2) and immobilized cell (black lines; compare to Fig. S4 F, example 1) out of  $n = 3$ . Bars: (C) 10  $\mu\text{m}$ ; (E, G, and H) 5  $\mu\text{m}$ .

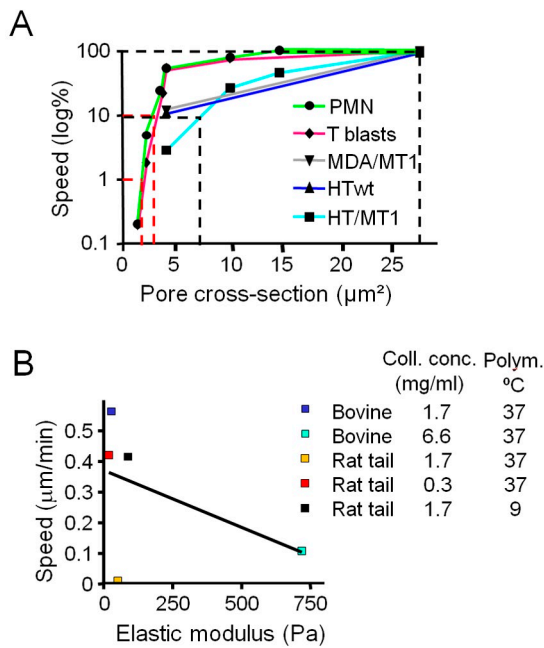


**Figure 6. Correlation of migration rates with pore cross section, but not scaffold stiffness.** (A) Migration rates as a function of pore cross section in mononuclear tumor cells, T-blasts, and PMN in rat tail collagen of different density in the presence of GM6001. Speed was normalized to the maximum speed in low-density matrix (0.3 mg/ml) as 100% reference, and the subtotal and absolute migration limits are indicated (dotted lines). Data points depict medians from Figs. 1 E, 2 D, 5 (B, D, and F); S2 G, and S4 A. For T-blasts and PMN, data points were included for additional pore size conditions,  $n = 2-4$ . Subtotal limits were reached at median pore cross sections of  $4-7 \mu\text{m}^2$  for tumor cells and  $3-4 \mu\text{m}^2$  for leukocytes, and absolute limits at  $2 \mu\text{m}^2$  for leukocytes. (B) Association of migration rates and elastic modulus of 3D collagen lattices. Speed medians were used from Fig. 2 (A, C, and E) obtained for cells migrating in the presence of GM6001 in lattice conditions for which the elastic modulus was measured (compare Fig. 1 C).  $R^2$  for linear regression (black line) was 0.2339 (nonsignificant).

With decreasing cross section, interfibrillar pores mechanically impede cell movement and impose deformation in a cell type-specific manner until net deformability is exceeded and the nucleus becomes mechanically trapped. This physical balance of translocation or arrest is modulated by “second-order” processes that control pore size or nucleus deformation. Here addressed effectors include (1) fibril remodeling by MT1-MMP to create “neo-space” and (2) mechanocoupling by integrins and actomyosin contractility to propel the nucleus forward through constraining spaces.

#### Variability of ECM porosity in vivo and in vitro

In vivo, fibrillar collagen is organized as fibrils and fibers of diverse caliber, orientation, and interfibrillar spacing (Starborg et al., 2008; Wolf et al., 2009). To reflect the variability of interfibrillar space present in loose versus dense interstitial tissues in vivo with ranges between 2 and  $30 \mu\text{m}$  (Stoitzner et al., 2002; Wolf et al., 2009; Weigelin et al., 2012), we similarly varied the median porosity of 3D collagen matrices. This space range serves to both guide and mechanically challenge moving cells that commonly display cross sections of  $30-100 \mu\text{m}^2$  in a cell type-dependent manner.

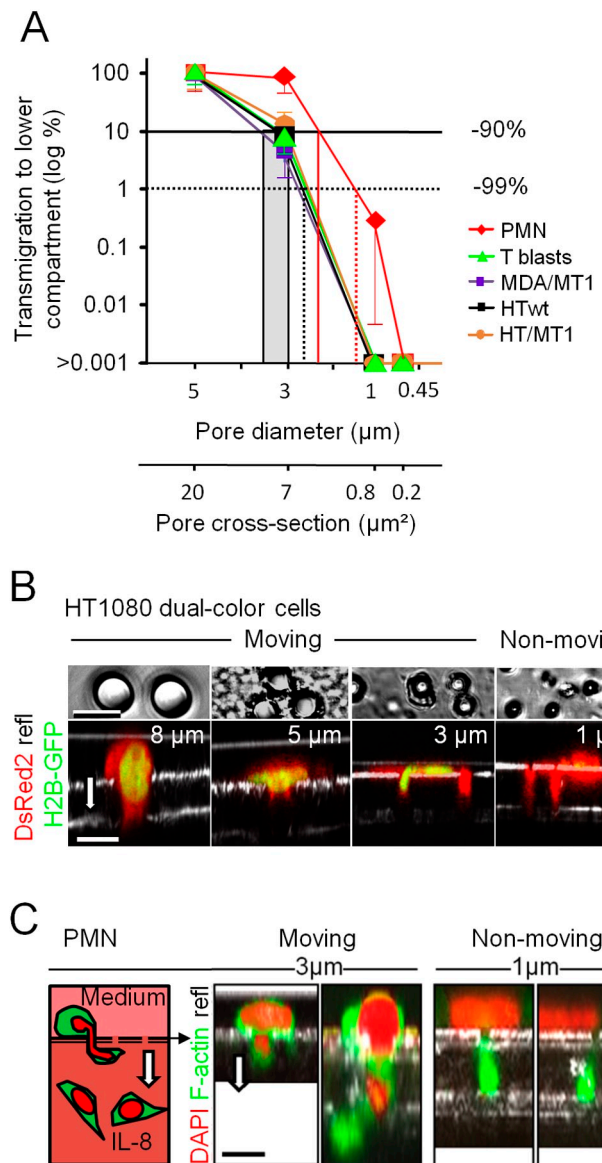


**Figure 7. Physical migration limits of mono- and polymorphonuclear cell types in transwell filter assay.** (A) Transmigration of different cell types through polycarbonate membranes of 5-, 3-, 1-, and  $0.45\text{-}\mu\text{m}$  pore diameter after 20 h (HT/MT1, HT/wt, and MDA/MT1 cells), 5 h (T-blasts) or 3 h (PMN). The cell number in the bottom compartment was normalized to transmigration through  $5\text{-}\mu\text{m}$  pores as 100% reference. Solid and dashed vertical lines represent the pore cross section at 90 and 99% inhibition, respectively, of migration for each cell type (black lines, mononuclear cells; gray area between black lines depicts a range of subtotal migration limits; red lines, PMN). Subtotal limits were reached at  $7-10 \mu\text{m}^2$  for tumor cells and T-blasts, and  $4 \mu\text{m}^2$  for PMNs; and absolute limits at  $5 \mu\text{m}^2$  for tumor cells and T-blasts and  $1-2 \mu\text{m}^2$  for PMNs ( $n = 3-5$ ; means, SD). (B) Polycarbonate membranes with pore sizes ranging from 8 to  $1 \mu\text{m}$  in diameter (top row). Representative images of nuclear deformation in transmigrating dual-color HT1080 cells and (C) PMNs during passage through pores of decreasing size. Filter membranes were fixed and, in C, stained as indicated ( $n = 2$ ). Arrows, direction of transmigration. Bars: (B)  $10 \mu\text{m}$ , (C)  $5 \mu\text{m}$ .

#### The biophysics of subtotal and absolute limits of cell migration

Our data show that migration speed diminishes as a linear function with decreasing pore size in a cell type-specific

Relative porosity	Migration efficacy	Nucleus				
		Mononuclear	CS ( $\mu\text{m}^2$ )	Polymorphonuclear	CS ( $\mu\text{m}^2$ )	CR
A		 Round / ellipsoid	Tu: 70 (50-100)  T: 30 (20-40)	 Partly unfolded	20	$\frac{1}{1}$
B		 Hourglass   Cigar-shaped	Tu: 7-70  T: 3-30	 Unfolded	2-20	$> \frac{1}{10}$
C		 Round / prolapse	Tu: < 7  T: < 3	 Collapsed / prolapse	< 2	$< \frac{1}{10}$
Maximum CR: CS compressed ( $\mu\text{m}^2$ ) / relaxed ( $\mu\text{m}^2$ )		Tu: 7 / 70	T: 3 / 30	PMN: 2 / 20		$\frac{1}{10}$

Modulators of migration rates near the physical limit include (1) pericellular proteolysis by MMPs that widens pore cross sections and (2) mechano-coupling toward ECM determining the force with which the nucleus is transported. CS, cross section; CR, compression ratio (degree of nuclear deformation versus nondeformed state); Tu, tumor cells; T, T blast; PMN, polymorphonuclear neutrophil. White arrows, direction of migration.

manner (Fig. 8). The decline in response to increasing mechanical confinement is not a simple “go or stop” decision, but is a gradual process that largely depends upon cell deformation, a coping strategy intrinsic to migrating cells (Lautenschläger et al., 2009; Wolf and Friedl, 2011; Tong et al., 2012). Maximum speed is reached at pore sizes that approximate the cell body where the substrate guides without physically impeding migration (Fig. 8 A; Jacobelli et al., 2010). With decreasing porosity, migration delay is reciprocal with increasing need for cell deformation, resulting in slower, but ongoing migration (Fig. 8 B, up to subtotal limit). Eventually, migration is abrogated when a cell type-specific maximum of deformation is reached (Fig. 8 C, absolute limit). As cell shape is highly adaptable, pores of defined cross sections, but distinct geometry, are equally well accommodated, including discontinuous polygonal-shaped pores in 3D fibrillar collagen, flat and broad cleft-like spaces, evenly shaped cylindrical pores in polycarbonate membranes, or elongated continuous channels in microdevices (Lautenschläger et al., 2009; Jacobelli et al., 2010; Rolli et al., 2010; Ilina et al., 2011; Balzer et al., 2012; Tong et al., 2012). A cross section of 20–30  $\mu\text{m}^2$  identified herein for near-optimal migration of HT1080 and MDA-MB-231 cells through complex-shaped spaces in collagen lattices and monomorphic transwell filter pores matches the 30  $\mu\text{m}^2$  cross-sectional areas of engineered rectangular microchannels that enable high migration speed (Tong et al., 2012). As an extreme example of shape adaptation, keratinocytes are able to traverse gaps of 500 nm in height but unrestricted in width (Brunner et al., 2006), confirming that the cross section of the transmigrated space, rather than its diameter, defines the efficacy of cell migration under confinement. Thus, the limits of cell migration are a two-parameter function of substrate porosity and cell deformability.

**Figure 8. Tissue porosity and nuclear deformation jointly determine subtotal and absolute limits of cell migration.** Cell migration efficacy is a joint function of substrate porosity and nuclear deformability, with MMP activity and mechano-coupling as modulators. (A) Minor deformation of nuclei and optimal velocity during migration through tissue of sufficient to high porosity, with mononuclear shapes in ellipsoid and polymorphonuclear nuclei in partly unfolded state. (B) Significant deformation of the nucleus and migration delay in cells moving through dense ECM with pore cross sections much below the nondeformed nucleus size. Mononuclear nuclei are compressed in their entirety and adopt hourglass-like or cigar-like shapes, whereas polymorphonuclear deformation consists of unfolding with transient pearl chain-like configuration as maximum. Maximal deformation is reached when the nucleus deforms to  $\sim 10\%$  of its original cross section, reaching a subtotal migration limit. (C) Migration arrest during confrontation with pore cross sections that exhaust the deformation capability of the nucleus. Both mono- and polymorphonuclear nuclei of migration-arrested cells retain a roundish, collapsed morphology with nonproductive transient prolapse, the cross section of which matches the geometry of the pore ( $\sim 5\text{--}10\%$  of the original nuclear cross section).

### The nucleus as a rate-limiting cell compartment

The nucleus is the largest and most rigid cell organelle, based on chromatin content and the stabilizing nuclear lamina, in particular lamin A/C (Dahl et al., 2004; Gerlitz and Bustin, 2011; Chow et al., 2012). Kinetic time-lapse imaging of migrating cells reveals two mechanically distinct forms of nuclear deformation: (1) the global deformation of mononuclear nuclei resulting in transient hourglass-like or cigar-shaped elongated morphologies, and (2) the unfolding of polymorphonuclear nuclei to adopt pearl chain-like configurations in the absence of major deformations in individual nuclear segments (Fig. 8). Albeit transient, these migration-associated nuclear morphologies are frequently detected in vivo during cancer cell dissemination (Yamauchi et al., 2005, 2006; Alexander et al., 2008; Beadle et al., 2008; Friedl et al., 2011) as well as transendothelial migration (Feng et al., 1998; Voisin et al., 2009). Whereas the deformability of the nucleus in dense space is finite, the cytoplasm is able to accommodate nearly any pore size used here, including 1- $\mu\text{m}^2$  gaps in collagen gels and 0.8- $\mu\text{m}^2$  pores of polycarbonate membranes (Schoumacher et al., 2010; Shankar et al., 2010).

Cell movement through dense ECM is impacted by at least three properties of the nucleus, including size, rigidity, and shape, which together control an adaptation range of factor 2–5 when mononuclear tumor cells and PMN are compared directly (Fig. 8). For all tested cell types, we noted a compellingly consistent ratio of minimum nuclear cross sections relative to undeformed state of  $\approx 1/10$  (Fig. 8, right column), suggesting that maximum compressibility is an absolute value irrespective of cell type, constitutive nuclear shape, or nuclear rigidity. The nuclear lamina may control nuclear shape and/or deformability rather than the absolute compression limit, which hints toward a

noncompressible intranuclear component (e.g., chromatin) in defining the compression maximum and, arguably, the physical limits of cell migration.

#### Modulation of ECM porosity by pericellular proteolysis

By degrading fibrillar collagen at the cell–matrix interface, MT1-MMP-dependent proteolysis widens collagen pore cross sections to accommodate the cell body and facilitates migration through degradable substrates (Wolf et al., 2007; Fisher et al., 2009; Sabeh et al., 2009). MT1-MMP thus accelerates migration at confining porosity above critical limits and, importantly, secures slow but nonetheless persistent migration even in very dense matrix. Conversely, with porosity high enough to accommodate the deforming cell body, pericellular proteolysis is dispensable and migration persists despite pharmacological or molecular targeting of MMP activity in either tumor cell or leukocyte populations (Fig. 8). MMPs thus act to modulate pore dimensions and thereby impact cell speed, deformation, and the limits of cell migration in biodegradable scaffolds. By establishing the preferential role of MMPs in pore size control, our approach using different collagen preparations side by side resolves controversies on the role of MMPs for cell invasion through 3D collagen scaffolds of different origin and porosity (Wolf et al., 2003a; Sabeh et al., 2004, 2009).

#### Modulation by mechanocoupling

Forces generated between cell and 3D scaffold impact cell deformation and migration through confined space (Fig. 8).  $\beta 1$  integrins that serve as both main adhesion receptors to fibrillar collagen and mechanotransducers in migrating cells (Huttenlocher et al., 1995; Puklin-Faucher and Sheetz, 2009) mediate the tractional forces needed to propel the nucleus through narrow pores. Likewise, Rho kinase-mediated actomyosin contractility reinforces integrin-mediated cell adhesion and controls retraction of the cell rear (Vicente-Manzanares et al., 2008) that together supports translocation of the nucleus through small spaces (Lämmermann et al., 2008). Thus, by using complementary mechanisms, MMP-dependent ECM degradation and integrin- and Rho-mediated force transmission jointly secure migration, particularly when space is restricted.

#### Parameters that affect the limits of cell migration indirectly

Additional physicochemical substrate properties likely impact migration rates, such as ECM telopeptide status and stiffness (Sabeh et al., 2009; Miron-Mendoza et al., 2010; Ehrbar et al., 2011). The high telopeptide content of collagen extracted from rat tails accelerates fibril polymerization and increases mechanical strength, but decreases fibril caliber and network porosity (Helseth and Veis, 1981; Elbjerrami et al., 2003; Sabeh et al., 2009; Wolf et al., 2009), which compromises nonproteolytic cell migration. Conversely, by temperature-dependently delaying collagen fibrillogenesis, larger pore sizes were generated that better matched nuclear size and deformability, and enabled MMP-independent cell movement. Thus, irrespective of the telopeptide content of the collagen preparation used, small

pores exhaust nuclear deformability and preclude MMP-independent migration. Our data further show no effect of substrate stiffness variation on cell immobilization by space constraints. The stiffness range used here includes 20–700 Pa for reconstituted fibrillar collagen and  $>10^6$  Pa for polycarbonate membranes, thus encompassing elastic modules of *in vivo* tissues, ranging from 200 to 1,000 Pa for mammary interstitium and from 1,000 to 10,000 Pa for adipocytes and myofibers (Stein et al., 2008; Butcher et al., 2009; Levental et al., 2009; Buxboim et al., 2010). Thus, when normalized to pore size, both soft and rigid substrates account for near-identical subtotal and absolute migration limits, excluding substrate stiffness above 20 Pa as an independent mechanism for controlling cell deformation or physical migration arrest.

#### Outlook

This multi-scale analysis of cell–matrix geometries and migration kinetics may serve as biophysical inventory and reference for addressing further modulators of cell migration in confined spaces. These likely include elasticity of the nucleus by regulation of lamin expression, the nucleus–cytoskeleton connection, intracellular and intranuclear pressure and hydration, chromatin organization, and physical “memory” as consequence of repetitive or long-lasting mechanical stress. Likely, the herein defined deformability of the cell body and nucleus matches the 2D and 3D tracks and gaps constitutively present in healthy connective tissues (Wolf et al., 2009; Weigelin et al., 2012). More complex invasion programs, however, may be required for penetration of tumor-associated collagen-rich desmoplastic tissue, scarred stroma, and, likely, basement membranes (Provenzano et al., 2006; Rowe and Weiss, 2009; Tanaka et al., 2010; Salmon et al., 2012). To this end, multi-scale wet-laboratory and *in silico* analyses of cell migration will jointly delineate the strategies used by cells to traverse ECM barriers encountered *in vitro* and *in vivo*.

## Materials and methods

#### Cell culture, cell purification, and reagents

The following cells were used: human HT1080-wild type (HT1080/wt or HT/wt) fibrosarcoma cells (ACC315; DSMZ Braunschweig); HT1080 cells transfected with MT1-MMP/MMP14 (HT1080/MT1 or HT/MT1; Deryugina et al., 1997); HT1080 dual-color cells expressing cytoplasmic DsRed2 and nuclear histone-2B (H2B)–coupled EGFP (Yamamoto et al., 2004); and human MDA-MB-231 breast cancer cells transfected with MT1-MMP (MDA-MB-231/MT1 or MDA/MT1; Moss et al., 2009). For generation of stable cell lines, the following constructs were generated: wild-type MT1-MMP protein in the eukaryotic expression vectors pcDNA3 and pCR3.1-Uni (Invitrogen) for HT1080 and MDA-MB-231 cell lines, respectively; wild-type RFP cDNA and H2B-GFP fusion gene in the retroviral pLNCX2 and pLHCX vectors (Takara Bio Inc.), all under the control of the cytomegalovirus promoter. Retroviral vectors were transfected into the packaging cell line PT67 prior to transduction of HT1080 cells. Cell lines were cultured (37°C at 5% CO<sub>2</sub> humidified atmosphere) in Dulbecco’s modified Eagle’s medium (DMEM; Invitrogen) supplemented with 10% heat-inactivated fetal calf serum (FCS; Sigma-Aldrich), 100 U/ml penicillin and 100 µg/ml streptomycin (PAA), 2 mM L-glutamine, and 1 mM sodium pyruvate (Invitrogen). Spheroids were generated by 24-h culture in low-adhesive culture dishes (Thermo Fisher Scientific) before incorporation into 3D collagen.

Human CD4+ T-blasts (T-blasts, purity  $>95\%$ , measured by flow cytometry) were obtained from healthy donors using the mononuclear cell fraction followed by stimulation with 1.25 µg/ml concanavalin A (Oncogene)

and 100 U/ml IL-2 (Strathman Biotech) in T-cell medium (TCM; RPMI 1640 medium [Gibco] supplemented as DMEM, except L-glutamine, and additionally with 10 mM Hepes [Gibco], 500 mM 2-mercaptoethanol, and 0.1 mM nonessential amino acids [Gibco]); and after 48 h were purified by positive immunomagnetic separation (Dynabeads) using paramagnetic beads coated with an anti-CD4+ mAb and magnetic separation from unbound cells. Human PMNs (purity >90%) were obtained by density gradient centrifugation (van Spriell et al., 2001). In brief, blood was added on top of two-layered histopaque and ficoll (Lymphoprep), centrifuged, and the PMN fraction isolated for immediate use in cell migration assays.

The following antibodies and reagents were used: polyclonal anti-collagen type I antibody (Rockland); polyclonal rabbit anti-COL23/4C<sub>short</sub> antiserum (IBEX Pharmaceuticals) or affinity purified rabbit antibody (ImmunoGlobe) directed against the C-terminal cleavage neo-epitope of collagens type I and type II (Wolf et al., 2007); function-blocking mouse monoclonal anti-β1 integrin IgG<sub>1</sub> (4B4; Coulter-Immunotech); isotypic IgG<sub>1</sub> control (NCG01; Thermo Fisher Scientific); monoclonal mouse anti-lamin A/C IgG<sub>1</sub> (131C3; Acris); monoclonal rabbit anti-GAPDH antibody (14C10; Cell Signaling Technology); polyclonal rabbit myosin light chain 2 and phospho-myosin light chain 2 (Thr18/Ser19) antibodies (Cell Signaling Technology); secondary goat anti-rabbit antibody conjugated to horseradish peroxidase (Thermo Fisher Scientific) or a fluorophore specific to the Odyssey system (IRDye 680RD; LI-COR Biosciences); secondary Alexa Fluor 647-conjugated preabsorbed goat anti-rabbit IgG (Invitrogen); Alexa Fluor 488-conjugated phalloidin (Invitrogen); DAPI (Roche); Hoechst 33342 (Invitrogen); GM6001 (ilomastat; EMD Millipore); protease inhibitor cocktail consisting of marimastat (50 μM; British Biotech), leupeptin (2 μM; Molecular Probes/Invitrogen), E-64 (50 μM; Sigma-Aldrich), aprotinin (0.7 μM; Sigma-Aldrich) and pepstatin A (50 μM; Sigma-Aldrich; Wolf et al., 2007); LPA (Sigma-Aldrich); Y-27632 (Sigma-Aldrich); and interleukin-8 (IL-8; R&D Systems). Knockdown of MT1-MMP by smart-pool siRNA (Thermo Fisher Scientific) was performed according to the manufacturer's protocol and as described previously (Wolf et al., 2007).

### 3D collagen matrix assays

Bovine dermal collagen was obtained as acidified, pepsinized solution (stock concentration 3.1 mg/ml; PureCol, Advanced BioMatrix); non-pepsinized (telopeptide intact) rat tail collagen was purified by acid extraction, stored in acidified lyophilized form (Hotary et al., 2000), and re-solubilized before use in 0.2% acetic acid. Fibrillar collagen matrices were reconstituted *in vitro* by raising the pH to 7.4 using either final concentrations of 0.345 N NaOH and buffering by 25 μM Hepes (Sigma-Aldrich) for rat tail matrices, or 0.75% Na-bicarbonate solution (Gibco) for bovine dermal lattices, together with minimum essential Eagle's medium (Sigma-Aldrich), and polymerized at 37°C, unless indicated otherwise (Hotary et al., 2000; Wolf et al., 2007). High-density matrices of bovine dermal collagen were reconstituted after concentration of the collagen solution (20 mg/ml; speed vac concentrator; Savant). Delayed polymerization speed of rat tail collagen was achieved by lowering the temperature during polymerization to 20, 14, or 9°C. Cell-free collagen lattices were used for bright-field microscopy (vertical invasion studies; Fig. S1 A), 3D confocal and electron microscopy, and atomic force microscopy. For cell migration assays, cells (20,000/100 μl) after detachment with EDTA (2 mM) or multicellular spheroids (2–7 spheroids/100 μl) were suspended in neutralized collagen solution before polymerization and incorporated into a self-constructed chamber (see Fig. S1 A). After addition of medium (containing 10% FCS) spontaneous migration was monitored, except for PMNs which were stimulated by 100 ng/ml IL-8. Inhibition experiments were performed using 20 μM GM6001, a five-component protease inhibitor cocktail, function-perturbing anti-β1 mAb 4B4, or Y-27632. Inhibitors were added to both the cell-collagen mixture and supernatant. For collagen contraction assays, cells (8 or 16 × 10<sup>4</sup>, for incubation with Y-27632 or 4B4, respectively) were incorporated into non-anchored bovine collagen lattices (300 μl) in 48-well plates.

### Collagen stiffness measurement

Fibrillar 3D matrices of rat tail or bovine dermal collagen were reconstituted and probed by atomic force microscopy in PBS on a Catalyst BioScope (Bruker Corporation) coupled to a confocal microscope (TCS SP5 II; Leica). A polystyrene microsphere (10-μm diameter; Polysciences, Inc.) was glued to a cantilever (NP-S type D nominal spring constant of 0.06 N/m; Bruker Corporation) by a two-component polyurethane glue (Bison International) and dried overnight. Individual spring constants were calibrated in PBS on glass by acquiring both deflection sensitivity and thermal noise data subsequently fitted and corrected for a V-shaped cantilever (te Riet et al., 2011).

Matrix stiffness was measured by repeatedly (2–20 times) bringing the bead-functionalized cantilever into contact with the surface of the lattice at an identical position (contact force ≤2 nN; approach–retraction distance 10 μm; approach velocity 10 μm/s) with a closed z-loop. Force–distance curves from each measurement were converted into force–indentation (F–δ) curves and subsequently fitted over the 0–1,500 pN force range with the Hertz model (Lin et al., 2007) using a custom algorithm (IgorPro 6; Wavemetrics) to calculate the stiffness:

$$F = \frac{4E\sqrt{R_c}}{3(1-\nu^2)} \cdot \delta^{\frac{3}{2}}$$

with  $F$ , force in Newtons [N];  $R_c$ , bead radius in meters [m];  $E$ , elastic modulus or stiffness in Pascals [Pa];  $\nu$ , Poisson ratio of 0.5; and  $\delta$ , penetration/indentation in meters [m].

### Time-lapse microscopy and quantification of cell migration

Cells were monitored by digital time-lapse, bright-field inverse microscopy (air objectives, 10×, NA 0.20; 20×, NA 0.30; 40×, NA 0.50; Leica) at 37°C using CCD cameras (Sentechn) and the 16-channel frame grabber software (Vistek) for 24 h with 4-min frame intervals (tumor cells) or for 2 h with 30-s intervals (leukocytes; Friedl and Bröcker, 2004). Migration speed was quantified by computer-assisted cell tracking (Autozell 1.0 software; Center for Computing and Communication Technologies [TZI], University of Bremen, Bremen, Germany) of xy paths with 12-min step intervals (tumor cells) or 30-s intervals (leukocytes). The average speed per cell was calculated from the length of the path divided by time, including “go” and “stop” phases.

### Confocal fluorescence and reflection microscopy and image analysis

Confocal microscopy (usually use of a 40×/NA 1.3 oil objective; LSM 510; Carl Zeiss) for 3D reconstruction of cell- and fixative-free hydrated matrices was performed with a minimum of 10 μm (typically 10–40 μm) distance to the cover glass. The pore dimensions were obtained from xy scans of cell-free native hydrated collagen lattices (1-μm slice interval; 30-μm z-depth) and orthogonal reconstruction as xz images. The pore cross sections were measured as areas free of dot-like reflection signal from collagen fibers, and pore diameters as smallest linear distance between two fibrils, as described previously (Friedl et al., 1997). For fixed-sample microscopy, cells migrating in 3D collagen matrix (drop matrix cultures; Fig. S1 A) were fixed (4% buffered PFA), washed, and stained with the indicated antibodies and dyes. Dynamic imaging of HT1080 dual-color cells or PMNs was performed as sequential z-stacks in drop collagen matrices within 12 h (HT1080) or 2 h (PMNs) after collagen polymerization using a temperature- and CO<sub>2</sub>-controlled stage (37°C, 5%). Neutrophil nuclei were labeled with live-DNA marker Hoechst 33342 (10 μg/ml). Time-lapse sequences were reconstructed as maximum intensity projections from usually each 2–3 fluorescence z-scans and 2 reflection scans (ImageJ; 1.40v; National Institutes of Health). Kymography of collagen fibril assembly was obtained from a maximum projection of three z-slices scanned continuously (37°C or 9°C; up to 120 min) and the polymerization speed was obtained from the mean signal intensity/frame. Images were processed by cropping, rotation, and manual adjustment of contrast and brightness and displayed in virtual colors. Elongation index (length/width) of moving cells was calculated from still images after 10 h of incubation. Non-moving, apoptotic or mitotic cells, as identified morphologically from the movie sequence, were excluded from elongation analysis. For cells treated with Y-27632 inhibitor, elongation was calculated only from cells that showed dendrite formation, measuring the main dendrite and, if present, a second dendrite that extended from the cell body by an angle more than 90° away from the main dendrite.

### Scanning/ transmission electron microscopy

For scanning and transmission electron microscopy (SEM, TEM), polymerized collagen lattices were fixed with 2% glutaraldehyde and dehydrated step-wise with ethanol of increasing concentration (30–100%). For SEM, samples were dehydrated by critical point drying using CO<sub>2</sub>, sputtered with gold and scanned (microscope JSM-6340F; JEOL). For TEM, samples were embedded in Epon (Serva), sliced, and imaged (transmission electron microscope 1010; JEOL).

### Western blotting

Lamin A/C content was determined by Western blot analysis from whole-cell lysates using anti-GAPDH mAb as loading control, followed by

chemiluminescence detection (ECL detection kit; GE Healthcare). pMLC<sup>T18519</sup> content was determined with MLC Ab as loading control, followed by fluorescence detection (Odyssey; LI-COR Biosciences) and densitometric analysis.

#### Filter transmigration assay

Transwell chambers with polycarbonate filters containing 5-, 3-, 1-, and 0.45- $\mu$ m diameter pore sizes (BD and Costar) were overlaid with cells and the transmigration conditions were as follows: tumor cells ( $10^4$ ; DMEM/2% FCS) migrated from the noncoated filter membrane into the lower chamber containing DMEM/10% FCS and pro-migratory lysophosphatidic acid (LPA;  $10\ \mu$ M); leukocytes ( $3 \times 10^5$ ; TCM/10% FCS) migrated from the filter membrane toward the lower compartment containing TCM/10% FCS, with precoating of type-I collagen on the lower membrane ( $40\ \mu$ g/ml; for CD4+ T-blasts) or addition of IL-8 ( $100\ \text{nM}$ ; for PMNs). Transmigration rates were counted as numbers of cells attached to the lower membrane side (tumor cells) or the total cell number in suspension in the lower compartment (CD4+ T-blasts, PMNs).

#### Statistics

Statistical analysis was performed by the two-tailed nonpaired Mann-Whitney test for samples with non-Gaussian distribution.

#### Online supplemental material

Fig. S1 introduces the 3D cell–collagen chamber systems used for stable collagen anchorage and confirms confocal reflection microscopy as the method of choice for structural imaging of collagen fibers. Fig. S2 visualizes and quantifies the porosity of collagen structures in vitro. Fig. S3 confirms maintenance or abrogation of cell migration in the presence of MMP inhibitor GM6001 or transient MT1-MMP knockdown for spheroid and vertical cell invasion. Fig. S4 presents speed and nuclear adaptation data from different cell types. Video 1 shows migration of single HT1080/MT1-MMP cells in bovine dermal and rat tail collagen in the absence or presence of MMP inhibitor GM6001. Video 2 shows a high-resolution confocal sequence of an arrested cell in rat tail collagen in the presence of GM6001. Video 3 is as Video 1, but for spheroids. Video 4 shows gradually increasing HT1080/MT1-MMP cell migration in rat tail collagen assembled at decreasing temperatures in the presence of MMP inhibitor GM6001. Video 5 shows nuclear deformation together with ongoing or abrogated migration of HT1080 cells transfected with histone H2B-GFP and cytoplasmic DsRed2 in the presence of protease inhibitors. Video 6 shows cells in the presence of MMP inhibitor GM6001 and cell traction modulators  $\beta$ 1 integrin 4B4 mAb or Y27632 in collagen gels of different pore sizes. Video 7 shows migration of CD4+ T blasts and PMNs (in the presence of chemokine IL-8) in the presence of MMP inhibitor GM6001 in rat tail collagen of varying concentration. Video 8 shows IL-8-enhanced migration of a neutrophil stained with nuclear marker Hoechst 33342 in rat tail collagen. Online supplemental material is available at <http://www.jcb.org/cgi/content/full/jcb.201210152/DC1>. Additional data are available in the JCB Data-Viewer at <http://dx.doi.org/10.1083/jcb.201210152.vv>.

We gratefully acknowledge M. Ott, F. Ogboro, and M. Zegers for technical support and advice; the Microscopical Imaging Centre core support by M. van Dommelen, M. Wijers, H. Croes, G.J. Bakker, and J. Fransen for assistance with imaging or data analysis; and M. Sharon Stack and E. Deryugina for providing MDA-MB-231 and HT1080 cells transfected with MT1-MMP.

This project was supported by the Netherlands Science Organization (NWO-VENI 680-47-421 to J. te Riet; NWO-VIDI 917.10.364 to K. Wolf; NWO-VICI 918.11.626 to P. Friedl), the European Union FP7 Tissue Transmigration Training Network (T3Net 237946 to P. Friedl); and the National Institutes of Health (R01 CA88308 and R01 CA71699 to S.J. Weiss).

Submitted: 31 October 2012

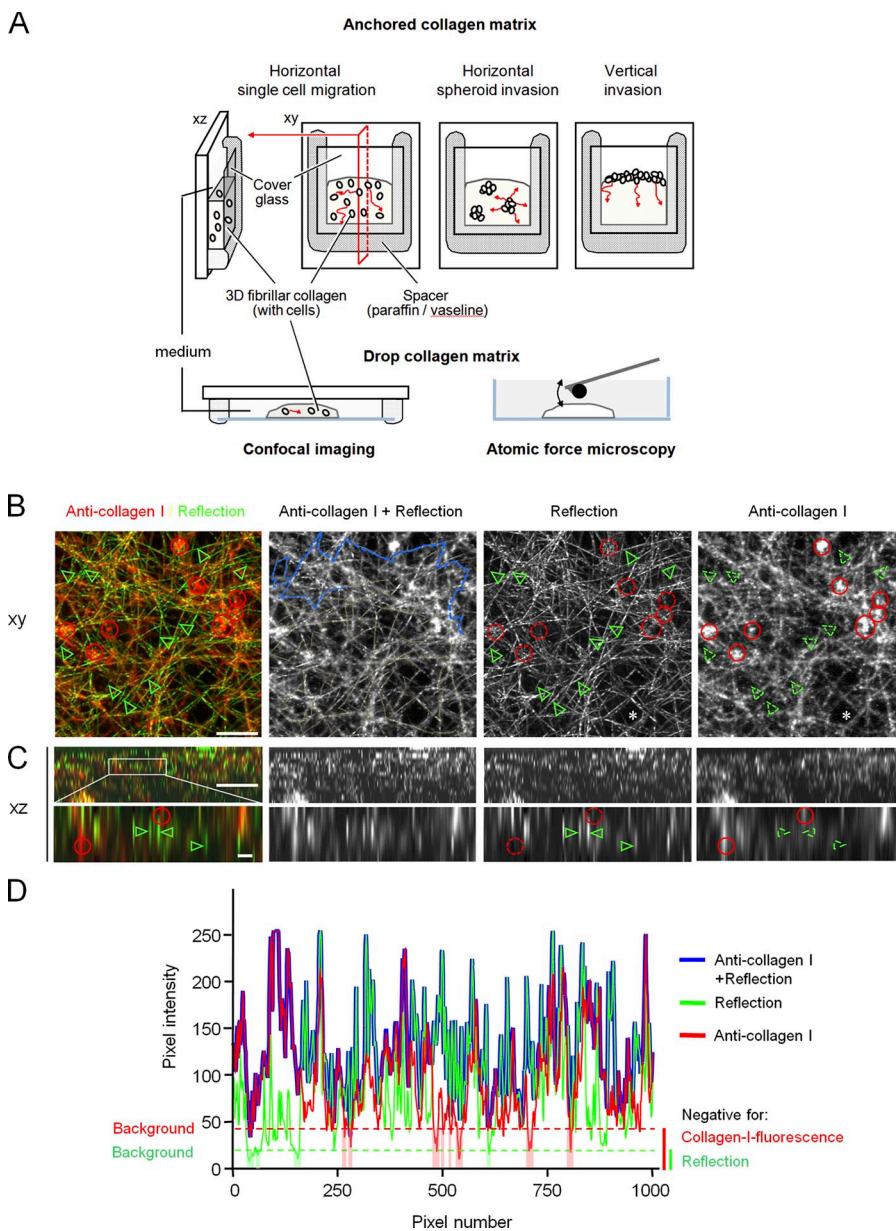
Accepted: 20 May 2013

## References

- Alexander, S., G.E. Koehl, M. Hirschberg, E.K. Geissler, and P. Friedl. 2008. Dynamic imaging of cancer growth and invasion: a modified skin-fold chamber model. *Histochem. Cell Biol.* 130:1147–1154. <http://dx.doi.org/10.1007/s00418-008-0529-1>
- Balzer, E.M., Z. Tong, C.D. Paul, W.C. Hung, K.M. Stroka, A.E. Boggs, S.S. Martin, and K. Konstantopoulos. 2012. Physical confinement alters tumor cell adhesion and migration phenotypes. *FASEB J.* 26:4045–4056. <http://dx.doi.org/10.1096/fj.12-211441>
- Beadle, C., M.C. Assanah, P. Monzo, R. Vallee, S.S. Rosenfeld, and P. Canoll. 2008. The role of myosin II in glioma invasion of the brain. *Mol. Biol. Cell.* 19:3357–3368. <http://dx.doi.org/10.1091/mbc.E08-03-0319>
- Berton, S., B. Belletti, K. Wolf, V. Canzonieri, F. Lovat, A. Vecchione, A. Colombatti, P. Friedl, and G. Baldassarre. 2009. The tumor suppressor functions of p27(kip1) include control of the mesenchymal/amoeboid transition. *Mol. Cell. Biol.* 29:5031–5045. <http://dx.doi.org/10.1128/MCB.00144-09>
- Brunner, C.A., A. Ehrlicher, B. Kohlstrunk, D. Knebel, J.A. Käs, and M. Goegler. 2006. Cell migration through small gaps. *Eur. Biophys. J.* 35:713–719. <http://dx.doi.org/10.1007/s00249-006-0079-1>
- Butcher, D.T., T. Alliston, and V.M. Weaver. 2009. A tense situation: forcing tumour progression. *Nat. Rev. Cancer.* 9:108–122. <http://dx.doi.org/10.1038/nrc2544>
- Buxboim, A., I.L. Ivanovska, and D.E. Discher. 2010. Matrix elasticity, cytoskeletal forces and physics of the nucleus: how deeply do cells ‘feel’ outside and in? *J. Cell Sci.* 123:297–308. <http://dx.doi.org/10.1242/jcs.041186>
- Chow, K.H., R.E. Factor, and K.S. Ullman. 2012. The nuclear envelope environment and its cancer connections. *Nat. Rev. Cancer.* 12:196–209.
- Dahl, K.N., S.M. Kahn, K.L. Wilson, and D.E. Discher. 2004. The nuclear envelope lamina network has elasticity and a compressibility limit suggestive of a molecular shock absorber. *J. Cell Sci.* 117:4779–4786. <http://dx.doi.org/10.1242/jcs.01357>
- Deryugina, E.I., G.X. Luo, R.A. Reisfeld, M.A. Bourdon, and A. Strongin. 1997. Tumor cell invasion through matrigel is regulated by activated matrix metalloproteinase-2. *Anticancer Res.* 17(5A):3201–3210.
- Ehrbar, M., A. Sala, P. Lienemann, A. Ranga, K. Mosiewicz, A. Bittermann, S.C. Rizzi, F.E. Weber, and M.P. Lutolf. 2011. Elucidating the role of matrix stiffness in 3D cell migration and remodeling. *Biophys. J.* 100:284–293. <http://dx.doi.org/10.1016/j.bpj.2010.11.082>
- Elbjerrami, W.M., E.O. Yonter, B.C. Starcher, and J.L. West. 2003. Enhancing mechanical properties of tissue-engineered constructs via lysyl oxidase crosslinking activity. *J. Biomed. Mater. Res. A.* 66:513–521. <http://dx.doi.org/10.1002/jbm.a.10021>
- Feng, D., J.A. Nagy, K. Pyne, H.F. Dvorak, and A.M. Dvorak. 1998. Neutrophils emigrate from venules by a transendothelial cell pathway in response to FMLP. *J. Exp. Med.* 187:903–915. <http://dx.doi.org/10.1084/jem.187.6.903>
- Fisher, K.E., A. Sacharidou, A.N. Stratman, A.M. Mayo, S.B. Fisher, R.D. Mahan, M.J. Davis, and G.E. Davis. 2009. MT1-MMP- and Cdc42-dependent signaling co-regulate cell invasion and tunnel formation in 3D collagen matrices. *J. Cell Sci.* 122:4558–4569. <http://dx.doi.org/10.1242/jcs.050724>
- Friedl, P., and S. Alexander. 2011. Cancer invasion and the microenvironment: plasticity and reciprocity. *Cell.* 147:992–1009. <http://dx.doi.org/10.1016/j.cell.2011.11.016>
- Friedl, P., and E.B. Bröcker. 2004. Reconstructing leukocyte migration in 3D extracellular matrix by time-lapse videomicroscopy and computer-assisted tracking. *Methods Mol. Biol.* 239:77–90.
- Friedl, P., and K. Wolf. 2009. Proteolytic interstitial cell migration: a five-step process. *Cancer Metastasis Rev.* 28:129–135. <http://dx.doi.org/10.1007/s10555-008-9174-3>
- Friedl, P., and K. Wolf. 2010. Plasticity of cell migration: a multiscale tuning model. *J. Cell Biol.* 188:11–19. <http://dx.doi.org/10.1083/jcb.200909003>
- Friedl, P., K. Maaser, C.E. Klein, B. Niggemann, G. Krohne, and K.S. Zänker. 1997. Migration of highly aggressive MV3 melanoma cells in 3-dimensional collagen lattices results in local matrix reorganization and shedding of alpha2 and beta1 integrins and CD44. *Cancer Res.* 57:2061–2070.
- Friedl, P., K. Wolf, and J. Lammerding. 2011. Nuclear mechanics during cell migration. *Curr. Opin. Cell Biol.* 23:55–64. <http://dx.doi.org/10.1016/j.ccb.2010.10.015>
- Gerlitz, G., and M. Bustin. 2011. The role of chromatin structure in cell migration. *Trends Cell Biol.* 21:6–11. <http://dx.doi.org/10.1016/j.tcb.2010.09.002>
- Goldberg, M.W., I. Huttenlauch, C.J. Hutchison, and R. Stick. 2008. Filaments made from A- and B-type lamins differ in structure and organization. *J. Cell Sci.* 121:215–225. <http://dx.doi.org/10.1242/jcs.022020>
- Grinnell, F., and W.M. Petroll. 2010. Cell motility and mechanics in three-dimensional collagen matrices. *Annu. Rev. Cell Dev. Biol.* 26:335–361. <http://dx.doi.org/10.1146/annurev.cellbio.042308.113318>
- Helseth, D.L. Jr., and A. Veis. 1981. Collagen self-assembly in vitro. Differentiating specific telopeptide-dependent interactions using selective enzyme modification and the addition of free amino telopeptide. *J. Biol. Chem.* 256:7118–7128.
- Hotary, K., E. Allen, A. Punturieri, I. Yana, and S.J. Weiss. 2000. Regulation of cell invasion and morphogenesis in a three-dimensional type I collagen matrix by membrane-type matrix metalloproteinases 1, 2, and 3. *J. Cell Biol.* 149:1309–1323. <http://dx.doi.org/10.1083/jcb.149.6.1309>

- Hotary, K.B., E.D. Allen, P.C. Brooks, N.S. Datta, M.W. Long, and S.J. Weiss. 2003. Membrane type I matrix metalloproteinase usurps tumor growth control imposed by the three-dimensional extracellular matrix. *Cell*. 114:33–45. [http://dx.doi.org/10.1016/S0092-8674\(03\)00513-0](http://dx.doi.org/10.1016/S0092-8674(03)00513-0)
- Huttenlocher, A., R.R. Sandborg, and A.F. Horwitz. 1995. Adhesion in cell migration. *Curr. Opin. Cell Biol.* 7:697–706. [http://dx.doi.org/10.1016/0955-0674\(95\)80112-X](http://dx.doi.org/10.1016/0955-0674(95)80112-X)
- Iliina, O., G.J. Bakker, A. Vasaturo, R.M. Hofmann, and P. Friedl. 2011. Two-photon laser-generated microtracks in 3D collagen lattices: principles of MMP-dependent and -independent collective cancer cell invasion. *Phys. Biol.* 8:015010. <http://dx.doi.org/10.1088/1478-3975/8/1/015010>
- Jacobelli, J., R.S. Friedman, M.A. Conti, A.M. Lennon-Dumenil, M. Piel, C.M. Sorensen, R.S. Adelstein, and M.F. Krummel. 2010. Confinement-optimized three-dimensional T cell amoeboid motility is modulated via myosin IIA-regulated adhesions. *Nat. Immunol.* 11:953–961. <http://dx.doi.org/10.1038/ni.1936>
- Jawerth, L.M., S. Münster, D.A. Vader, B. Fabry, and D.A. Weitz. 2010. A blind spot in confocal reflection microscopy: the dependence of fiber brightness on fiber orientation in imaging biopolymer networks. *Biophys. J.* 98:L1–L3. <http://dx.doi.org/10.1016/j.bpj.2009.09.065>
- Lämmermann, T., B.L. Bader, S.J. Monkley, T. Worbs, R. Wedlich-Söldner, K. Hirsch, M. Keller, R. Förster, D.R. Critchley, R. Fässler, and M. Sixt. 2008. Rapid leukocyte migration by integrin-independent flowing and squeezing. *Nature*. 453:51–55. <http://dx.doi.org/10.1038/nature06887>
- Lautenschläger, F., S. Paschke, S. Schinkinger, A. Bruel, M. Beil, and J. Guck. 2009. The regulatory role of cell mechanics for migration of differentiating myeloid cells. *Proc. Natl. Acad. Sci. USA*. 106:15696–15701. <http://dx.doi.org/10.1073/pnas.0811261106>
- Levental, K.R., H. Yu, L. Kass, J.N. Lakins, M. Egeblad, J.T. Erler, S.F. Fong, K. Csiszar, A. Giaccia, W. Weninger, et al. 2009. Matrix crosslinking forces tumor progression by enhancing integrin signaling. *Cell*. 139:891–906. <http://dx.doi.org/10.1016/j.cell.2009.10.027>
- Lin, D.C., E.K. Dimitriadis, and F. Horkay. 2007. Robust strategies for automated AFM force curve analysis—I. Non-adhesive indentation of soft, inhomogeneous materials. *J. Biomech. Eng.* 129:430–440. <http://dx.doi.org/10.1115/1.2720924>
- Miron-Mendoza, M., J. Seemann, and F. Grinnell. 2010. The differential regulation of cell motile activity through matrix stiffness and porosity in three dimensional collagen matrices. *Biomaterials*. 31:6425–6435. <http://dx.doi.org/10.1016/j.biomaterials.2010.04.064>
- Moss, N.M., Y.I. Wu, Y. Liu, H.G. Munshi, and M.S. Stack. 2009. Modulation of the membrane type I matrix metalloproteinase cytoplasmic tail enhances tumor cell invasion and proliferation in three-dimensional collagen matrices. *J. Biol. Chem.* 284:19791–19799. <http://dx.doi.org/10.1074/jbc.M109.020362>
- Packard, B.Z., V.V. Artym, A. Komoriya, and K.M. Yamada. 2009. Direct visualization of protease activity on cells migrating in three-dimensions. *Matrix Biol.* 28:3–10. <http://dx.doi.org/10.1016/j.matbio.2008.10.001>
- Provenzano, P.P., K.W. Eliceiri, J.M. Campbell, D.R. Inman, J.G. White, and P.J. Keely. 2006. Collagen reorganization at the tumor-stromal interface facilitates local invasion. *BMC Med.* 4:38. <http://dx.doi.org/10.1186/1741-7015-4-38>
- Puklin-Faucher, E., and M.P. Sheetz. 2009. The mechanical integrin cycle. *J. Cell Sci.* 122:179–186. <http://dx.doi.org/10.1242/jcs.042127>
- Raub, C.B., V. Suresh, T. Krasieva, J. Lyubovitsky, J.D. Mih, A.J. Putnam, B.J. Tromberg, and S.C. George. 2007. Noninvasive assessment of collagen gel microstructure and mechanics using multiphoton microscopy. *Biophys. J.* 92:2212–2222. <http://dx.doi.org/10.1529/biophysj.106.097998>
- Ren, X.D., R. Wang, Q. Li, L.A. Kahek, K. Kaibuchi, and R.A. Clark. 2004. Disruption of Rho signal transduction upon cell detachment. *J. Cell Sci.* 117:3511–3518. <http://dx.doi.org/10.1242/jcs.01205>
- Ridley, A.J., M.A. Schwartz, K. Burridge, R.A. Firtel, M.H. Ginsberg, G. Borisy, J.T. Parsons, and A.R. Horwitz. 2003. Cell migration: integrating signals from front to back. *Science*. 302:1704–1709. <http://dx.doi.org/10.1126/science.1092053>
- Rolli, C.G., T. Seufferlein, R. Kemkemer, and J.P. Spatz. 2010. Impact of tumor cell cytoskeleton organization on invasiveness and migration: a microchannel-based approach. *PLoS ONE*. 5:e8726. <http://dx.doi.org/10.1371/journal.pone.0008726>
- Rowe, R.G., and S.J. Weiss. 2009. Navigating ECM barriers at the invasive front: the cancer cell-stroma interface. *Annu. Rev. Cell Dev. Biol.* 25:567–595. <http://dx.doi.org/10.1146/annurev.cellbio.24.110707.175315>
- Sabeh, F., I. Ota, K. Holmbeck, H. Birkedal-Hansen, P. Soloway, M. Balbin, C. Lopez-Otin, S. Shapiro, M. Inada, S. Krane, et al. 2004. Tumor cell traffic through the extracellular matrix is controlled by the membrane-anchored collagenase MT1-MMP. *J. Cell Biol.* 167:769–781. <http://dx.doi.org/10.1083/jcb.200408028>
- Sabeh, F., R. Shimizu-Hirota, and S.J. Weiss. 2009. Protease-dependent versus -independent cancer cell invasion programs: three-dimensional amoeboid movement revisited. *J. Cell Biol.* 185:11–19. <http://dx.doi.org/10.1083/jcb.200807195>
- Salmon, H., K. Franciszkiwicz, D. Damotte, M.C. Dieu-Nosjean, P. Validire, A. Trautmann, F. Mami-Chouaib, and E. Donnadieu. 2012. Matrix architecture defines the preferential localization and migration of T cells into the stroma of human lung tumors. *J. Clin. Invest.* 122:899–910. <http://dx.doi.org/10.1172/JCI45817>
- Sanz-Moreno, V., G. Gadea, J. Ahn, H. Paterson, P. Marra, S. Pinner, E. Sahai, and C.J. Marshall. 2008. Rac activation and inactivation control plasticity of tumor cell movement. *Cell*. 135:510–523. <http://dx.doi.org/10.1016/j.cell.2008.09.043>
- Schoumacher, M., R.D. Goldman, D. Louvard, and D.M. Vignjevic. 2010. Actin, microtubules, and vimentin intermediate filaments cooperate for elongation of invadopodia. *J. Cell Biol.* 189:541–556. <http://dx.doi.org/10.1083/jcb.200909113>
- Shankar, J., A. Messenberg, J. Chan, T.M. Underhill, L.J. Foster, and I.R. Nabi. 2010. Pseudopodial actin dynamics control epithelial-mesenchymal transition in metastatic cancer cells. *Cancer Res.* 70:3780–3790. <http://dx.doi.org/10.1158/0008-5472.CAN-09-4439>
- Sodek, K.L., M.J. Ringuette, and T.J. Brown. 2007. MT1-MMP is the critical determinant of matrix degradation and invasion by ovarian cancer cells. *Br. J. Cancer*. 97:358–367. <http://dx.doi.org/10.1038/sj.bjc.6603863>
- Sodek, K.L., T.J. Brown, and M.J. Ringuette. 2008. Collagen I but not Matrigel matrices provide an MMP-dependent barrier to ovarian cancer cell penetration. *BMC Cancer*. 8:223. <http://dx.doi.org/10.1186/1471-2407-8-223>
- Starborg, T., Y. Lu, K.E. Kadler, and D.F. Holmes. 2008. Electron microscopy of collagen fibril structure in vitro and in vivo including three-dimensional reconstruction. *Methods Cell Biol.* 88:319–345. [http://dx.doi.org/10.1016/S0091-679X\(08\)00417-2](http://dx.doi.org/10.1016/S0091-679X(08)00417-2)
- Stein, A.M., D.A. Vader, L.M. Jawerth, D.A. Weitz, and L.M. Sander. 2008. An algorithm for extracting the network geometry of three-dimensional collagen gels. *J. Microsc.* 232:463–475. <http://dx.doi.org/10.1111/j.1365-2818.2008.02141.x>
- Stoitzner, P., K. Pfaller, H. Stössel, and N. Romani. 2002. A close-up view of migrating Langerhans cells in the skin. *J. Invest. Dermatol.* 118:117–125. <http://dx.doi.org/10.1046/j.0022-202x.2001.01631.x>
- Tanaka, Y., K. Matsuo, and S. Yuzuriha. 2010. Long-term histological comparison between near-infrared irradiated skin and scar tissues. *Clin Cosmet Investig Dermatol.* 3:143–149. <http://dx.doi.org/10.2147/CCID.S15729>
- te Riet, J., A.J. Katan, C. Rankl, S.W. Stahl, A.M. van Buul, I.Y. Phang, A. Gomez-Casado, P. Schön, J.W. Gerritsen, A. Cambi, et al. 2011. Interlaboratory round robin on cantilever calibration for AFM force spectroscopy. *Ultramicroscopy*. 111:1659–1669. <http://dx.doi.org/10.1016/j.ultramicro.2011.09.012>
- Tong, Z., E.M. Balzer, M.R. Dallas, W.C. Hung, K.J. Stebe, and K. Konstantopoulos. 2012. Chemotaxis of cell populations through confined spaces at single-cell resolution. *PLoS ONE*. 7:e29211. <http://dx.doi.org/10.1371/journal.pone.0029211>
- van Spruiel, A.B., J.H. Leusen, M. van Egmond, H.B. Dijkman, K.J. Assmann, T.N. Mayadas, and J.G. van de Winkel. 2001. Mac-1 (CD11b/CD18) is essential for Fc receptor-mediated neutrophil cytotoxicity and immunologic synapse formation. *Blood*. 97:2478–2486. <http://dx.doi.org/10.1182/blood.V97.8.2478>
- Vicente-Manzanares, M., M.A. Koach, L. Whitmore, M.L. Lamers, and A.F. Horwitz. 2008. Segregation and activation of myosin IIB creates a rear in migrating cells. *J. Cell Biol.* 183:543–554. <http://dx.doi.org/10.1083/jcb.200806030>
- Voisin, M.B., A. Woodfin, and S. Nourshargh. 2009. Monocytes and neutrophils exhibit both distinct and common mechanisms in penetrating the vascular basement membrane in vivo. *Arterioscler. Thromb. Vasc. Biol.* 29:1193–1199. <http://dx.doi.org/10.1161/ATVBAHA.109.187450>
- Weigel, B., G.J. Bakker, and P. Friedl. 2012. Intravital third harmonic generation microscopy of collective melanoma cell invasion: Principles of interface guidance and microvesicle dynamics. *IntraVital*. 1:32–43. <http://dx.doi.org/10.4161/intv.21223>
- Wolf, K., and P. Friedl. 2011. Extracellular matrix determinants of proteolytic and non-proteolytic cell migration. *Trends Cell Biol.* 21:736–744. <http://dx.doi.org/10.1016/j.tcb.2011.09.006>
- Wolf, K., I. Mazo, H. Leung, K. Engelke, U.H. von Andrian, E.I. Deryugina, A.Y. Strongin, E.B. Bröcker, and P. Friedl. 2003a. Compensation mechanism in tumor cell migration: mesenchymal-amoeboid transition after blocking of pericellular proteolysis. *J. Cell Biol.* 160:267–277. <http://dx.doi.org/10.1083/jcb.200209006>
- Wolf, K., R. Müller, S. Borgmann, E.B. Bröcker, and P. Friedl. 2003b. Amoeboid shape change and contact guidance: T-lymphocyte crawling through fibrillar collagen is independent of matrix remodeling by MMPs

- and other proteases. *Blood*. 102:3262–3269. <http://dx.doi.org/10.1182/blood-2002-12-3791>
- Wolf, K., Y.I. Wu, Y. Liu, J. Geiger, E. Tam, C. Overall, M.S. Stack, and P. Friedl. 2007. Multi-step pericellular proteolysis controls the transition from individual to collective cancer cell invasion. *Nat. Cell Biol.* 9:893–904. <http://dx.doi.org/10.1038/ncb1616>
- Wolf, K., S. Alexander, V. Schacht, L.M. Coussens, U.H. von Andrian, J. van Rheenen, E. Deryugina, and P. Friedl. 2009. Collagen-based cell migration models in vitro and in vivo. *Semin. Cell Dev. Biol.* 20:931–941. <http://dx.doi.org/10.1016/j.semcdb.2009.08.005>
- Yamamoto, N., P. Jiang, M. Yang, M. Xu, K. Yamauchi, H. Tsuchiya, K. Tomita, G.M. Wahl, A.R. Moossa, and R.M. Hoffman. 2004. Cellular dynamics visualized in live cells in vitro and in vivo by differential dual-color nuclear-cytoplasmic fluorescent-protein expression. *Cancer Res.* 64:4251–4256. <http://dx.doi.org/10.1158/0008-5472.CAN-04-0643>
- Yamauchi, K., M. Yang, P. Jiang, N. Yamamoto, M. Xu, Y. Amoh, K. Tsuji, M. Bouvet, H. Tsuchiya, K. Tomita, et al. 2005. Real-time in vivo dual-color imaging of intracapillary cancer cell and nucleus deformation and migration. *Cancer Res.* 65:4246–4252. <http://dx.doi.org/10.1158/0008-5472.CAN-05-0069>
- Yamauchi, K., M. Yang, P. Jiang, M. Xu, N. Yamamoto, H. Tsuchiya, K. Tomita, A.R. Moossa, M. Bouvet, and R.M. Hoffman. 2006. Development of real-time subcellular dynamic multicolor imaging of cancer-cell trafficking in live mice with a variable-magnification whole-mouse imaging system. *Cancer Res.* 66:4208–4214. <http://dx.doi.org/10.1158/0008-5472.CAN-05-3927>
- Yang, Y.L., and L.J. Kaufman. 2009. Rheology and confocal reflectance microscopy as probes of mechanical properties and structure during collagen and collagen/hyaluronan self-assembly. *Biophys. J.* 96:1566–1585. <http://dx.doi.org/10.1016/j.bpj.2008.10.063>
- Yang, Y.L., S. Motte, and L.J. Kaufman. 2010. Pore size variable type I collagen gels and their interaction with glioma cells. *Biomaterials.* 31:5678–5688. <http://dx.doi.org/10.1016/j.biomaterials.2010.03.039>
- Zaman, M.H., L.M. Trapani, A.L. Sieminski, D. Mackellar, H. Gong, R.D. Kamm, A. Wells, D.A. Lauffenburger, and P. Matsudaira. 2006. Migration of tumor cells in 3D matrices is governed by matrix stiffness along with cell-matrix adhesion and proteolysis. *Proc. Natl. Acad. Sci. USA.* 103:10889–10894. <http://dx.doi.org/10.1073/pnas.0604460103>

Wolf et al., <http://www.jcb.org/cgi/content/full/jcb.201210152/DC1>

merged fibrils consists of 1,000 pixels (see D) and illustrates the region of interest for image segmentation (totalling 7,177 pixels). (D) Pixel intensities of merged image as reference (blue), reflection (green), and fluorescence (red) channel. Signal-negative regions below background (intensity threshold: 20 pixel for reflection, green dotted line; 45 pixel for fluorescence, red dotted line) are displayed as shaded lines. Of 7,177 pixels analyzed, 97.2% were positive for reflection signal, and 90% for fluorescence signal. One representative experiment out of  $n = 2$ . Bars, 10  $\mu\text{m}$  (except xz zooms, 1  $\mu\text{m}$ ).

**Figure S1. 3D collagen models for cell migration analysis, optical imaging, and measurement of stiffness.** (A) (Top row) Cell-collagen mixtures were polymerized in vertical chamber position to ensure that cells slowly sinking downward during collagen assembly remained embedded within the 3D collagen scaffold and did not reach the collagen-glass interface (Friedl and Bröcker, 2004). The dual-glass interface further provided sufficient adsorption and anchorage of the collagen matrix to the chamber, preventing cell-mediated matrix contraction or spontaneous collapse of upper matrix layers in the vertical invasion assay. Cell migration was measured in three different assays: (1) migration of single cells embedded during collagen polymerization; (2) invasion from 3D multicellular spheroids embedded during collagen polymerization; or (3) vertical invasion from the top of a preformed 3D collagen lattice. Red arrows, cell migration tracks. (Bottom row) Drop gels embedded in closed chambers were used for confocal imaging of both fixed and live cell-collagen cultures (left), whereas drop gels in an open Petri dish were used for atomic force microscopy using a bead-functionalized cantilever (right). (B–D) Validation of confocal reflection microscopy for detecting collagen fibrils. (B) Merged and single-channel images of anti-collagen type-I immunofluorescence staining and reflection signal from hydrated 3D collagen fibril structures for comparison of loss of signal. 3D bovine collagen (1.7 mg/ml) was fixed with paraformaldehyde, stained with polyclonal rabbit anti-collagen type-I antibody, and scanned by confocal microscopy. xy images represent maximum intensity projections of three consecutive z-scans with each 2- $\mu\text{m}$  distance. (C) Overview xz images and zoom of central regions. (B and C) To estimate the proportion of false-negative pixels using confocal reflection microscopy, anti-collagen staining and reflection signals were both cross-referenced for signal-negative regions. Red circles show fluorescence-positive (smooth line) but reflection-negative (dotted line) dots, consistent with rare fibrils oriented in vertical direction (Jawerth et al., 2010). Green arrowheads, reflection-positive fibrils (smooth line) with fluorescence signal below background (dotted line). Background was determined from fibril-free areas (asterisks). Blue line along

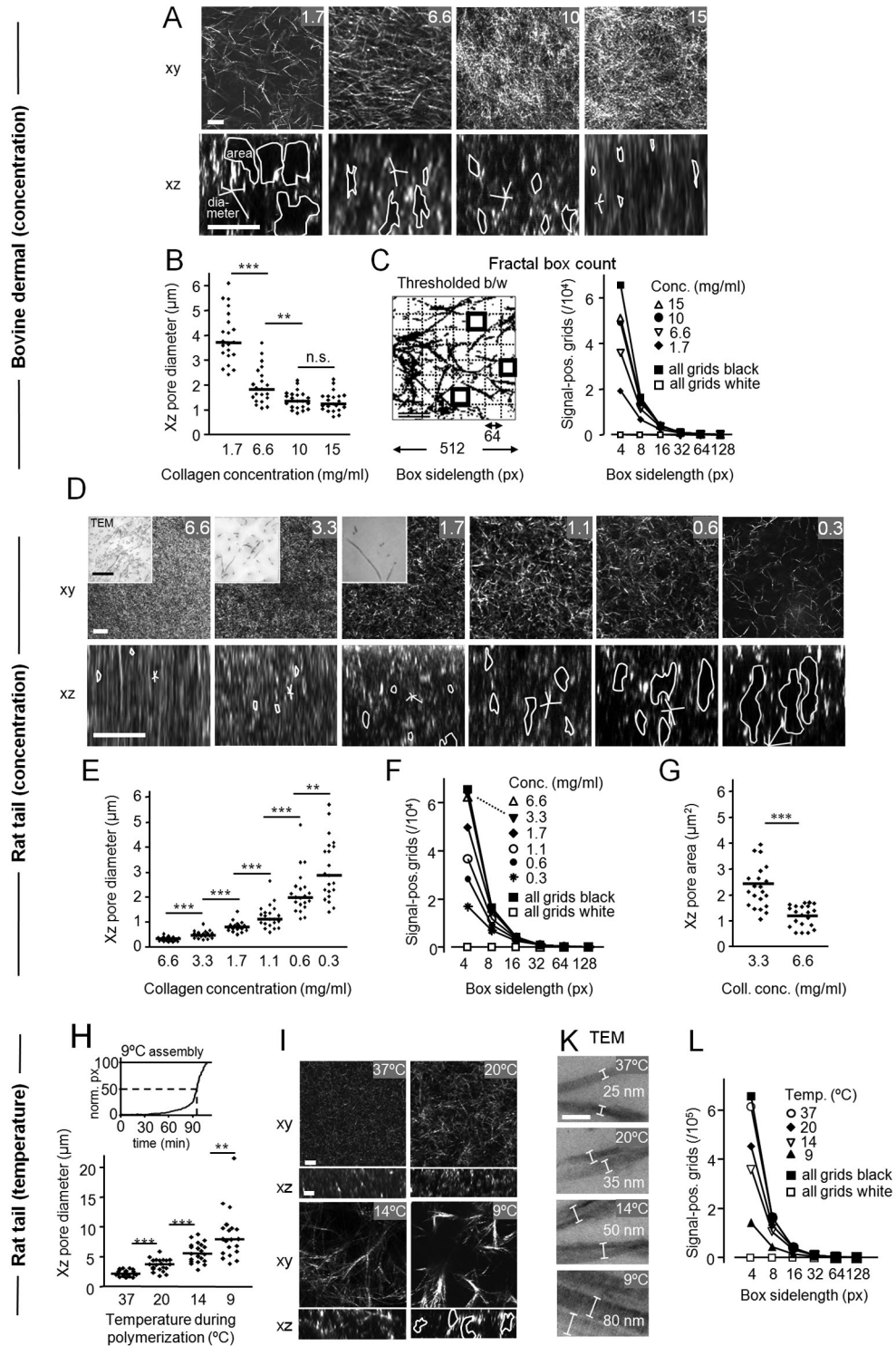


Figure S2. **Quantification of fibril organization and density of 3D collagen matrices reconstituted from bovine dermal and rat tail collagen.** (A, D, and I) Single xy and xz reflection scans from native hydrated collagen lattices used for image analysis. In xz scans, marked areas indicate examples of measured pore areas, and straight lines show examples of pore diameters. (B, E, and H [bottom]) Pore diameters obtained from xz sections (medians representing 21 data points per condition;  $n = 2$ ). (C, F, and L) Overall porosity, quantified by fractal analysis from single xy sections. Fractal box count was performed by overlaying a thresholded image with grids decreasing in side length. Only those grid-encircled boxes were counted that contain reflection-positive signal, as a reciprocal measure for porosity (fractal box count plugin, Fiji software). (G) Pore cross sections for high-density rat tail collagen, calculated from xz images in D. (C, F, G, and L) One representative analysis out of  $n = 2-3$ . (D [insets] and K) Transmission electron microscopy images of collagen fibrils and fibers after polymerization at different concentration and temperature. (H, top) Assembly speed of rat tail collagen (1.7 mg/ml) at 9°C and half-maximum polymerization (dashed lines; after 96 min). \*\*\*,  $P < 0.001$ ; \*\*,  $P < 0.01$ ; n.s., nonsignificant. Bars, 10  $\mu\text{m}$  (all images) except 1  $\mu\text{m}$  (D, insets) and 0.1  $\mu\text{m}$  (K).

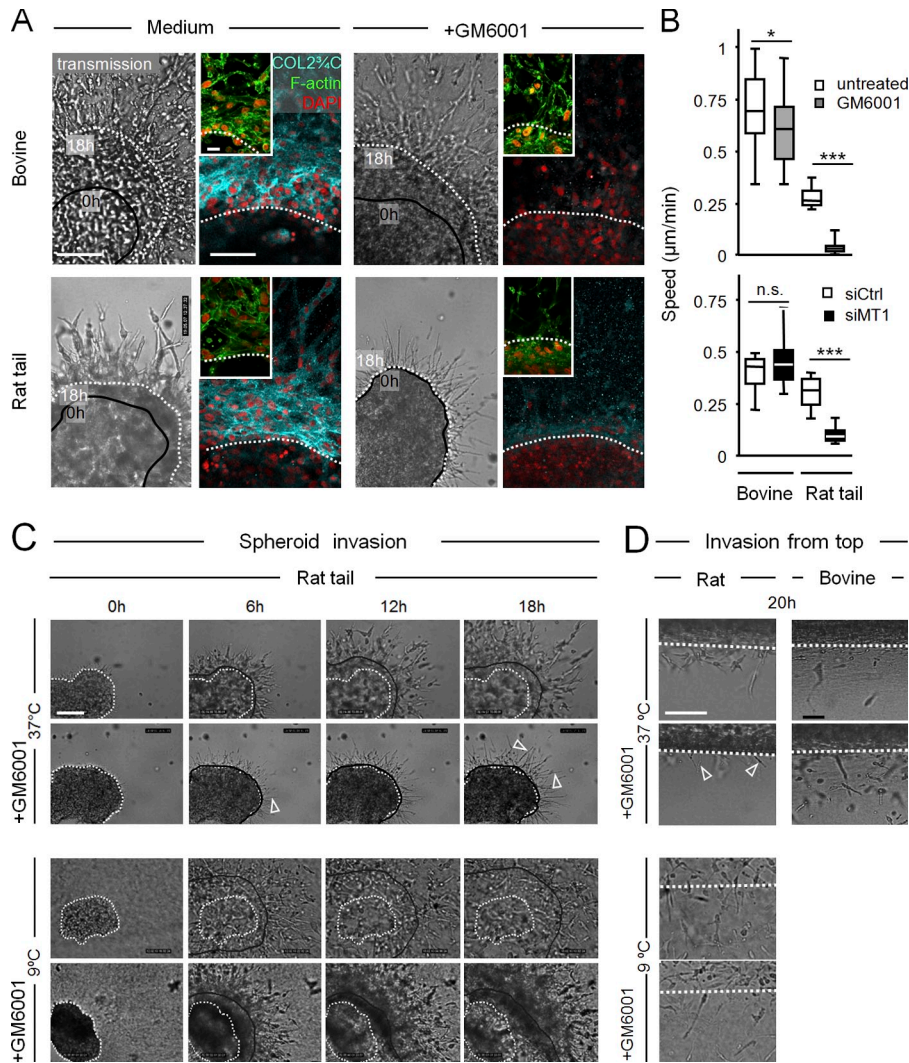


Figure S3. **Rate-limiting conditions of cell migration in 3D spheroid and vertical invasion assays.** (A) HT1080/MT1 spheroid invasion into bovine dermal or rat tail collagen (1.7 mg/ml) after 24 h in the absence or presence of MMP inhibitor GM6001. Black lines (transmission images) indicate tumor–collagen borders at 0 h (after collagen polymerization); white dashed lines show the noninvasive edge of the spheroids after 18 h migration, consistent with abrogation of proliferation in confining matrices in the absence of MMP activity (Hotary et al., 2003). Images are part of the time-lapse sequences shown in Video 3. For fluorescence imaging, samples were fixed with PFA, stained with DAPI, phalloidin, or COL23/4C<sub>short</sub> Ab, three-dimensionally reconstructed by confocal microscopy, and displayed as maximum intensity projection. (B) Cell migration speed after emigration from spheroids into bovine dermal or rat tail collagen in the absence or presence of GM6001 (top), or after transient RNA knockdown of MT1-MMP (bottom). Box and whiskers represent the mean population speed per cell with median, 25th/75th, and 5th/95th percentiles (15–20 cells from one representative experiment). \*\*\*,  $P < 0.0001$ ; \*,  $P < 0.05$ ; n.s., nonsignificant. (C) Spheroid invasion or (D) vertical invasion into rat tail collagen polymerized at 37°C or 9°C in the absence or presence of GM6001. As reference, vertical invasion into bovine dermal collagen was equally effective in the presence or absence of GM6001. Arrowheads indicate long cytoplasmic extensions as indicator for abrogated migration despite frustraneous leading edge dynamics. Bars, 100 µm (all images) except 20 µm (A, inset).

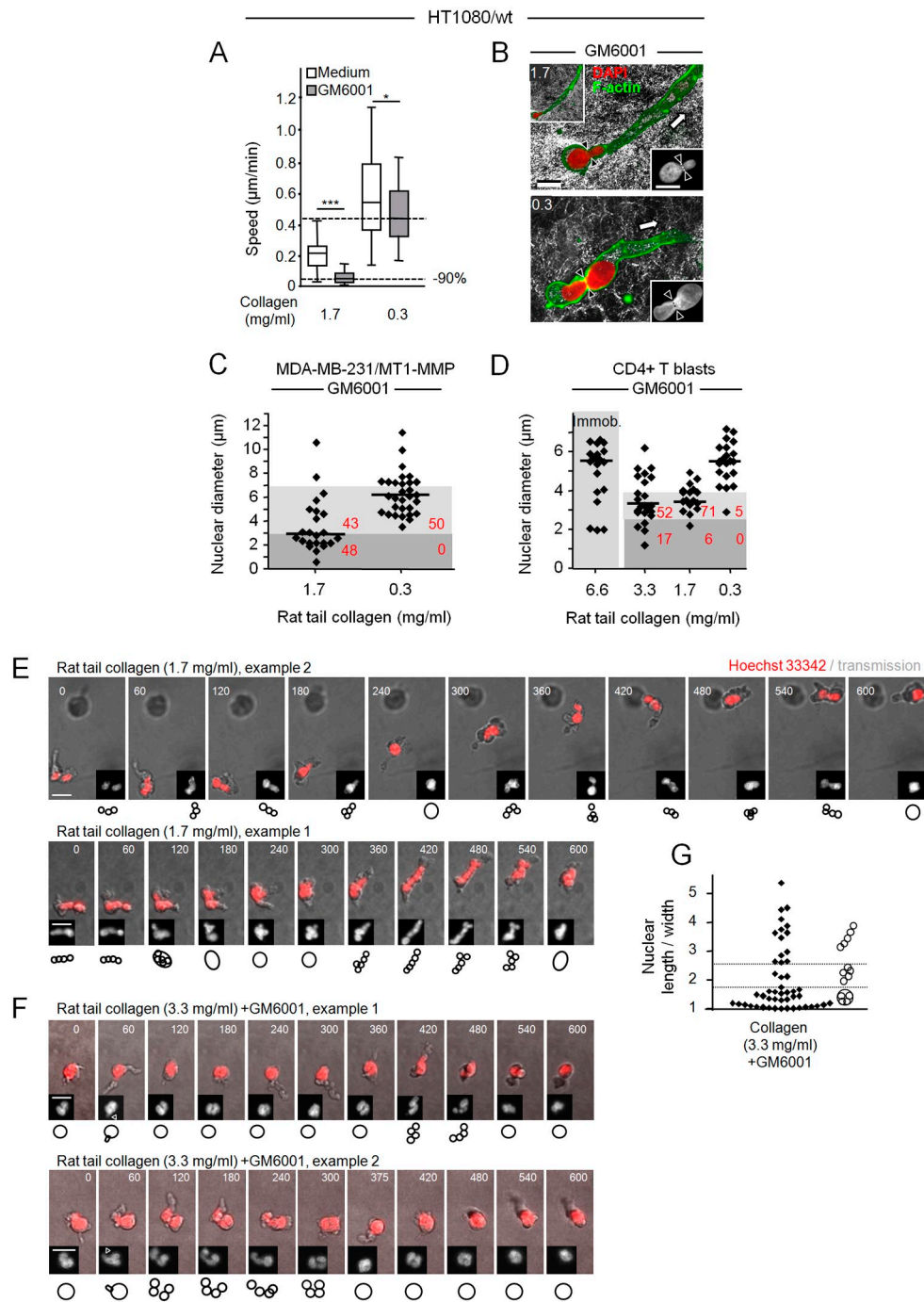
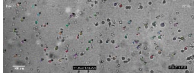
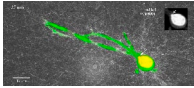


Figure S4. **Speed and nuclear adaptation data from different cell types.** Limits of MMP-independent migration and nuclear morphologies in HT1080/wt (A and B), MDA-MB-231/MT1 cells (C), CD4+ T-blasts (D), and PMNs (E-G). (A) Migration rates of HT1080/wt cells in the absence or presence of GM6001 in low- or high-density rat tail collagen. Top dashed line in A, 100% reference for MMP-independent migration; bottom dashed line, 90% inhibition of migration ( $n = 4$ ). \*\*\*,  $P < 0.0001$ ; \*,  $P < 0.05$ . (B) Cellular including nuclear morphologies in HT1080/wt cells. Prolapse of the nucleus in direction of a prominent dendrite-like leading extension at conditions of migration arrest (1.7 mg/ml), whereas hour-glass shaped nuclear morphology is retained in moving cell (0.3 mg/ml). Arrowheads, region of nuclear deformation. Arrows, direction of cell protrusion or migration. (C and D) Deformation of nuclei in MDA-MB-231/MT1 cells (C) and CD4+ T-blasts (D) in low- or high-density rat tail collagen in the presence of GM6001 ( $n = 2$ , each 17–30 nuclei). Dark gray areas correspond to nuclei of immobilized cells. (E and F) Bright-field time-lapse sequences of PMNs stained with DNA marker Hoechst 33342 during migration in rat tail collagen of 1.7 (E) or 3.3 mg/ml (F) in the absence or presence of GM6001. Insets (grayscale) show the Hoechst channel (maximum intensity projections of three z-planes with 2- $\mu\text{m}$  step size); symbols indicate the nuclear conformation and arrowheads indicate prolapse. (G) Length/width index of polymorphonuclear nuclei at high rat tail collagen density (3.3 mg/ml) that strongly decreased but did not abrogate migration in the presence of GM6001 (compare Fig. 4 F), showing the spectrum of nuclear shapes in slowly moving PMNs. 49 cells,  $n = 2$ . Bars, 10  $\mu\text{m}$ .

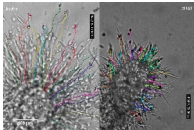
Video 1. **Spontaneous migration of HT1080/MT1 cells, and migration arrest after inhibition of MMP activity by GM6001 in 3D rat tail but not bovine dermal collagen.** Imaging by bright-field inverse microscopy (Leica) at 37°C. (A, first sequence) Overview movies of spontaneous HT1080/MT1 cell movement in bovine dermal (left) and rat tail collagen of 1.7 mg/ml (right); representative still images are shown in Fig. 2, A and C. Second clip: as first, plus 20  $\mu$ M GM6001. Cell tracks indicate the migratory capacity of each condition. Time (h:min:s) as indicated (24-min intervals over 18 h of observation).



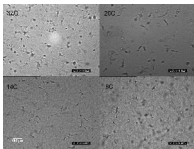
Video 2. **Confocal time sequence of migration arrest.** Single HT1080/dual-color cell expressing cytoplasmic DsRed2 (red) and nuclear histone-2B (H2B)-coupled EGFP (green) in rat tail collagen (1.7 mg/ml), in the presence of GM6001. White arrow highlights short-lived repeated prolapses of the nucleus in direction of the leading pseudopod. Imaging at 37°C by laser scanning confocal microscopy (510; Carl Zeiss) and maximum intensity projection of confocal z-stacks with 2.5-min time interval for 100 min.



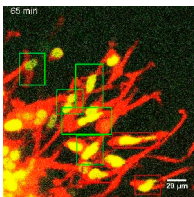
Video 3. **Emigration of HT1080/MT1 cells from multicellular spheroids into bovine (left) or rat (right) collagen (1.7 mg/ml) in the absence (A, first sequence) or presence (B, second sequence) of MMP inhibitor GM6001 with paths representing the position change of cell centers.** Representative still images are shown in Fig. S3 A. Bright-field inverse microscopy (Leica) at 37°C; time (h:min:s) as indicated (16-min intervals over 8.5 h of observation).



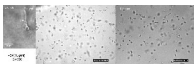
Video 4. **Rescue of MMP-independent migration of HT1080/MT1 cells in rat tail collagen (1.7 mg/ml) in the presence of GM6001 after reconstitution at different polymerization temperatures indicated in the movies.** Bright-field inverse microscopy (Leica) at 37°C. Time (h:min:s) as indicated (32-min intervals over 22 h of observation).

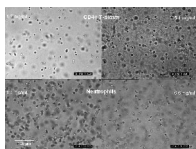


Video 5. **Nuclear deformation together with ongoing or abrogated migration of HT1080 cells transfected with histone H2B-GFP and cytoplasmic DsRed2 in the presence of protease inhibitors.** Deformation of the nucleus in spheroid culture of HT1080 dual-color cells expressing cytoplasmic DsRed2 (red) and nuclear histone-2B (H2B)-coupled EGFP (green) during migration (cells in green boxes) or immobilization (red boxes) in bovine collagen (6.6 mg/ml) in the presence of MMP and other protease inhibitors (see Materials and methods). Imaging at 37°C by confocal microscopy (SP2; Leica); maximum intensity projection of confocal z-stacks; 5-min frame rate, 85-min observation time.

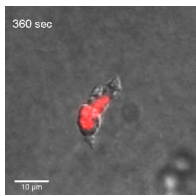


Video 6. **Abrogation and physical rescue of nonproteolytic HT1080/MT1 cell migration after interference with cell-matrix adhesion and contractility in bovine dermal collagen lattices of increasing pore sizes.** Imaging at 37°C by bright-field inverse microscopy (Leica). Cells migrating in the presence of GM6001 were additionally treated with 4B4 mAb (1  $\mu$ g/ml; A, first video sequence) or Y-27632 (2  $\mu$ M; B, second sequence). (A and B) Left, collagen concentration 1.7 mg/ml (high magnification); middle, 1.7 mg/ml; right, 0.8 mg/ml. Time intervals as indicated.





Video 7. **Migration of CD4<sup>+</sup> T-blasts and PMNs in rat tail collagen at low and high concentrations indicated in the movie in the presence of MMP-inhibitor GM6001.** Imaged at 37°C by bright-field inverse microscopy (Leica); time (h:min:s) as indicated (2-min frame interval; 2 h of observation).



Video 8. **Pearl chain configuration of segmented nucleus during neutrophil migration in rat tail collagen (1.7 mg/ml) in the presence of IL-8 (100 ng/ml).** Maximum intensity projection of red DNA label (Hoechst 33342 dye) with transmission image obtained by time-lapse confocal microscopy (LSM510; Carl Zeiss). Frame interval, 15 s; duration, 10 min.

## References

- Friedl, P., and E.B. Bröcker. 2004. Reconstructing leukocyte migration in 3D extracellular matrix by time-lapse videomicroscopy and computer-assisted tracking. *Methods Mol. Biol.* 239:77–90.
- Hotary, K.B., E.D. Allen, P.C. Brooks, N.S. Datta, M.W. Long, and S.J. Weiss. 2003. Membrane type I matrix metalloproteinase usurps tumor growth control imposed by the three-dimensional extracellular matrix. *Cell*. 114:33–45. [http://dx.doi.org/10.1016/S0092-8674\(03\)00513-0](http://dx.doi.org/10.1016/S0092-8674(03)00513-0)
- Jawerth, L.M., S. Münster, D.A. Vader, B. Fabry, and D.A. Weitz. 2010. A blind spot in confocal reflection microscopy: the dependence of fiber brightness on fiber orientation in imaging biopolymer networks. *Biophys. J.* 98:L1–L3. <http://dx.doi.org/10.1016/j.bpj.2009.09.065>